JULIUS-MAXIMILIANS-UNIVERSITAET WUERZBURG
FAKULTAET FUER PHYSIK UND ASTRONOMIE
LEHRSTUHL FUER ASTRONOMIE

MASTER THESIS

Joint X-ray and Radio Observations of the Quasar 4C+74.26

Author:	Stefan Lindeholz
Supervisors:	Prof. Dr. Matthias Kadler
Date of Submission:	May 3, 2021

Zusammenfassung

Aktive Galaxienkerne (AGN) gehoeren zu den hellsten Quellen die in unserem Universum beobachtet werden koennen. Diese koennen ueber das gesamte elektromagnetische Spektrum beobachtet werden, dabei wird die helle Strahlung durch Akkretion eines Supermassiven Schwarzen Lochs erzeugt. Die erzeugte Energie wird dann ueber Synchroton- und inverse Compton Streuungsprozesse abgestrahlt. Das Roentgenspektrum wird noch durch zusaetzliche Effekte beeinflusst, was zum einen durch Absorption und zum anderen durch relativistische Reflektion geschieht, um die wichtigsten Effekte zu nennen. Einige AGN besitzen Jets, welche Stroeme hochrelativistischen Materials sind, die durch starke Magnetfelder kollimiert werden. In diesen Jets befinden sich knotenartige Strukturen, die hellere Punkte sind, die detektiert und lokalisiert werden koennen. Diese Knoten wandern entlang der Jet-Achse nach aussen und die scheinbare Geschwindigkeit kann bestimmt werden. Diese kann sich dabei ueber der Lichtgeschwindigkeit befinden aufgrund eines Projektionseffektes. Die AGN Jets sind symmetrisch und besitzen oftmals einen Gegen-Jet der sich in entgegengesetzte Richtung bewegt. Dies kann an dem Quasar $4C + 74.26$ beobachtet werden, der einen schwachen Gegen-Jet besitzt. Der Gegen-Jet wird durch den Beaming-effekt abgeschwaecht waehrend der Jet selber verstaerkt wird. Um diese Jets im Radiobereich zu untersuchen, bedarf es der Technik der Very Long Baseline Interferometry (VLBI, Interferometrie von sehr langen Basislinien), was uns erlaubt die Aufloesung zu verbessern. Diese hoehere Aufloesung ist notwendig um die innersten Strukturen der AGN aufzuloesen. Das wird mittels verschieden entfernter Teleskope gemacht, deren Signale miteinander Korreliert werden. In diesem Fall wurde das Very Long Baseline Array (VLBA) verwendet, welches verschiedene Teleskope in Nord Amerika besitzt die dort verteilt sind. Die Beobachtungsfrequenz des Instruments betraegt dabei $15\,\mathrm{GHz}$.

Im Bereich der Roentgenstrahlung sind Beobachtungen auf der Erdoberflaeche nicht moeglich, da die Erdatmosphaere keine Roentgenstrahlung durchlaesst. Daher ist es notwendig Satelliten in den Erdorbit zu stationieren und von dort aus zu beobachten. *NuSTAR* und *Swift* sind dabei die hier verwendeten Roentgenteleskope die insgesamt einen Energiebereich von $0.5\,\mathrm{keV}$ bis $80\,\mathrm{keV}$ erfassen, mittels der Wolter-Teleskop Technologie.

$4C + 74.26$ wurde in sieben Radioepochen in einem Zeitraum von September 2016 bis Abril 2019 beobachtet, sowie in einer Roentgenkampagne in 2014. Die Roentgendaten wurden von ein paar Gruppen ausgewertet, die Analyse der Kinematik der Quelle wurde noch nicht veroeffentlicht. Die Radiodaten wurden hinsichtlich ihrer Kinematik untersucht und mit vorlaeufigen Vorschungsergebnissen verglichen, was zu insgesamt drei ver-

schiedenen Szenarien gefuehrt hat. Das Roentgenspektrum wurde mittels einer Kombination verschiedener Modelle analysiert, bestehend aus *relxill*, *pexmon* und Galaktischer Absorption, beruhend auf frueheren Analysen (Lohfink et al., 2017). Fuer die scheinbare Geschwindigkeit der Komponenten des Jets haben sich Geschwindigkeien von $\beta_{app1} = 1,886$, $\beta_{app2} = 0.76$ und $\beta_{app3} = 0.58$ ergeben, je nachdem welches Szenario herangezogen wurde. Um letztendlich Erkentnisse zu gewinnen ueber das wahrscheinlichste Radio-Szenario wurde eine weitere Epoche analysiert, die waehrend der Bearbeitung im Juni 2020 aufgenommen wurde. Diese wurde entsprechend ausgewertet und mit dem bestehenden Modell verglichen, und hat sich dabei als konsistent erwiesen. Zusaetzlich wurde in der neuen Epoche eine weitere Komponente gefunden. Am Ende haben sich zwei Szenarien als moeglich erwiesen die jeweils einen Inklinationswinkel zur Jet-Achse von $\Phi_1 = 47\,\mathrm{deg}$ und $\Phi_2 = 18\,\mathrm{deg}$ ergeben.

Abstract

Active Galactic Nuclei (AGN) are among the brightest sources throughout our Universe and can be observed over the whole electromagnetic spectrum. The bright radiation is caused by accretion of mass into a super-massive black hole (SMBH) leading to synchrotron radiation and inverse Compton scattering processes. In the X-ray regime the spectrum gets further influenced where the most prominent effects are absorption and relativistic reflection effects,but some smaller effects take place as well. Some AGN feature jets, which are streams of highly relativistic matter, collimated through strong magnetic fields. Those jets posses knotty features, which are bright spots and can be detected and localized. Those features propagate along the jet axis and the apparent speed can be tracked. This speed can be above the speed of light, because of an projection effect. The AGN jets are symmetrical and often times a counter jet can be observed moving in the opposite direction. This can be observed at the Quasar 4C + 74.26, where a jet is moving towards the observer and the counterjet is faintly visible, which is because of the effect of beaming.

These jets can be studied using Very Long Baseline Interferometry (VLBI), a technique used for increasing the resolution and thus resolving the inner structure of the AGN. This is done by stationing telescopes away from each other and correlating their signals. Here this was done with the very large baseline array (VLBA), which is stationed throughout North America and observing at a frequency of 15 GHz.

In the X-ray regime ground based observations are not possible, because of the atmosphere and the instruments are operated in space. *NuSTAR* and *Swift* are X-ray telescopes observing energy bands from 0.5 keV to 80 keV with Wolter telescopes.

4C + 74.26 was observed in seven radio epochs from 2016 to 2019 and in an X-ray campaign in 2014. While the X-ray observations has been researched by some groups, the kinematic of the source is not published yet. Therefore, the radio epochs has been analysed and compared with preliminary data, which has lead to three different radio scenarios. The X-ray spectrum has been researched with an model combination of *relxill*, *pexmon* and galactic absorption which resulted from previous results(Lohfink et al., 2017). For the apparent speed of the jet components $\beta_{app1} = 1,886$, $\beta_{app2} = 0.76$ and $\beta_{app3} = 0.58$ could be derived, based on the considered scenario. To further gain insights of the final radio scenario, a newly taken observation from June 2020, has also been analysed and compared to the model, which is consistent with the found scenario in this thesis. Also a new ejected jet component has been found in the new observation. In the end two scenarios remain valid, where an inclination angle of the jet axis can be calculated to $\Phi_1 = 47 \deg$ and $\Phi_2 = 18 \deg$.

Contents

Contents

1. Scientific Background

Humankind shared always a fascination in the seemingly limitless possibilities of our universe. It started with observations of celestial objects with the bare eye, but with improved tools more information about the night sky objects could be collected. A large step towards modern astronomy started in the 20th century as Karl Jansky noticed unknown Radio signals, which he could not explain at that time. The signals originated somewhere in the universe and it became a quest for astronomers to study the sky in the new light of events. With the development of spacecraft and orbital observation stations, it is now possible to study our sky over the whole electromagnetic spectrum. Some remarkable sources to study are active galactic nuclei (AGN), which emit radiation over the whole electromagnetic spectrum. This will be in the following observed in the Quasar 2043+749 or 4C 74.26, which has been observed in the X-ray by the *NuSTAR*-satellite and the *Swift*-satellite in 2014. Studies were conducted by Lohfink et al. (2017) and Bhatta et al. (2018) to investigate the interaction between the accretion disc reflection properties and the radio-jet as proposed by A. P. Marscher (2009). The main purpose of this chapter is to gain some insight in what kind of object the source 2043+749 is. In addition, the principal physics behind the observational methods used for the analysis will be discussed in this chapter. Two regimes of the electromagnetic spectrum are of importance for this thesis: radio emission observed with VLBI (Very-Long-Baseline-Interferometry), and X-ray emission measured with the *NuSTAR*-satellite *Swift*-satellites.

1.1. Active Galactic Nuclei

The first evidence that there is something strange with some galaxies was found by Carl Seyfert as he studied optical radiation of galaxies. The optical emission normally was emitted by a superposition of stars and therefore thermal, but some additional features in the spectrum showed signs that there are indeed unknown bright sources emitting radiation in those galaxies. Later it was clear that there are galaxies, which posses an supermassive black hole (SMBH) that accretes mass and converting the enormous energy released in this process into radiation. In fact now it is clear that all galaxies are centered around blackholes, but the distinction to those active ones is that they do not accrete mass and thus are not producing this large amounts of radiation. Active Galactic Nuclei (AGN) were first discovered in the optical regime where the extremely red-shifted lines in the spectrum indicated a very great distance to the source, which needs a bright

luminosity to be detected. Later, radio-, X-ray- and γ-ray observations could be assigned to those objects, confirming that they indeed produce very high luminosities, but do emit radiation over the whole electromagnetic spectrum aswell and thus differ from normal galactic nuclei. This leads to the question what radiative processes are involved and what powers them. Another important feature which some of the active galaxies posses, is a collimated outflowing plasma which shows on large scale in the radio regime and is hence called a radio-jet. Based on the strength of the luminosity, emission-line profiles and the radio jet, a rough morphological categorization can be done by Urry and Padovani (1995) in their unification model.

In this section the different properties and types of AGN will be discussed with a priority on Quasars, the type of class which is associated with 2043+749. They will be put into context with the unification model. There will be a short introduction on inverse Compton scattering, synchrotron emission, absorption and Thompson scattering, since those are the most prominent radiation mechanisms involved in emission of AGN. In addition the relativistic effect of superluminal motion will be introduced. The information in the following section is mostly based on the books of Beckmann and Shrader (2012) and Kembhavi and Narlikar (1999) and is noted otherwise if separate sources are involved.

1.1.1. Subclasses of AGN

As already mentioned there are several subclasses of AGN based on some characteristic physical properties. It was noticet by Seyfert (1943) that the emission lines of AGN were highly redshifted, which indicates a large distance to the emitting source. Since the received radiation declines with the second order of the distance, these sources had to be very bright. But the strength of the luminosity can vary in AGN and can be used to identify the type of AGN, as well as studying the emission line profiles.

Seyfert Galaxies, the most common class of AGN in our local universe. These are relatively close for AGN allowing a very good inspection of their spectra and they can be further distinguished based on their highly ionized emission lines. Type 1 shows broad and narrow line features in the spectra Type 2 only narrow lines and Type 0 no lines at all. The narrow lines are the Balmer-lines caused by high abundance of hydrogen. Seyfert galaxies are not associated with radio jets and therefore appear radio quiet.

Another class of AGN which are also hard to detect are those who show very low luminosity. Since it was discovered that our own host galaxy is centered by a SMBH through measuring the radio source Sagitarius A*. This indicates that there are many similar cases of galaxies, where the central SMBH is not visible through bright luminosities. In the Milky Way the black-hole is starved out or converts the energy of the accretion rather inefficiently and therefore does not emit large energies identifying AGN. Those sources fill the gap between the active and the inactive galactic nuclei and are known as **low-ionization emission line regions** (Liner). These show faint core luminosities and strong emission lines and tend to share some properties with the Seyfert 2 galaxies. Based on the classification of Kellermann et al. (1989)

$$R_{\mathrm{r-o}} = \frac{S_{\mathrm{r}}}{S_{\mathrm{o}}}, \tag{1.1.1}$$

an AGN is considered to be radio-loud if the ratio of the radio flux R_{r} to the optical flux R_{o} is larger then 10. Radio-quiet AGN typically show ratios between 0.1 and 1. This leads to the further subclasses of **Radio Galaxies** which are similar to the Seyfert galaxies in optical light. They can also be classified along their optical spectra as broad-line-radio galaxies and narrow-line-radio-galaxies. Based on their luminosity they can be distinguished further as done by Fanaroff and Riley (1974). Fanaroff-Riley Type 1(FR1) galaxies show low luminosity and a bright nucleus extracting two broad radio jets which end in plumes, whereas FR Type 2 show high luminosity and one-sided jets which end in radio lobes.

Similar to the radio galaxies one can go ahead and classify AGN based on their properties in the X-ray regime, where the **Ultraluminous X-ray sources** (ULX) excel. To put them in contrast in the X-ray regime they tend to appear 10 times super-Eddington for galactic x-ray binaries. They are reasonably newly discovered since most of them got discovered by Chandra in 2004. They tend to have simple X-ray spectra with most of them fit to a power-law spectrum or a power-law added by a thermal absorption component.

Some AGN span a new subclass of AGN in the Infra-red by having high luminosity in the regime, the so called **ultra-luminous infra-red galaxies** (ULIRGs).

The next class can also be split up in several subclasses. In the late 1950s to 1960s large sky surveys were performed in the radio regime. Through following optical observations new objects were found which appeared like blue stars. Normal stars will not be measured in the radio regime, with the only exception being our sun due to the close proximity. Due to the analogy they were called **quasi-stellar radio sources**(Quasars). They have also strong emission lines, but are highly red shifted. With more sensitive observations the gaps between the Seyfert galaxies could be filled with intermediate objects. Based on the newly found properties further distinctions were possible. The search for those object was made easier by the blue color in the optical regime which expands in the UV-range. A feature that is called big blue bump and is caused by the accretion of the disc. Quasars are the brightest sources of the AGN and thus can be detected from very far. Quasars are the Objects with the highest redshifts measured throughout the Universe.

Although they were first detected in the radio regime radio-quiet Quasars exist as well. They are harder to detect than their radio counterparts but are way more numerous than the radio-loud ones. Around 90% of all quasars are radio-quiet, but keep in mind that that radio emission can still exist according to the definition of radio-loudness above. Typical features for Quasars are a variable continuum flux, a strong UV component and broad emission lines. The highly luminous radio sources can be distinguished based on their radio profile. There are the **Flat Spectrum Radio Quasars**(FSRQ) and the **Steep Spectrum Radio Quasars**(SSRQ) where the ladder are dominated by radio

Radio loud?	AGN Type	Subtype	X-ray absorbed	Broad Lines?	Narrow Lines?	FeKα	γ-rays
RL							
	Radio Galaxy						
		NLRG	Yes	Yes	Yes	No	No
		BLRG	No	Yes	Yes	Yes	Few
		FR I/II	No	Some	Yes	No	No
	Quasar	Type 1	No	Yes	Yes	Yes	Some
	Quasar	Type 2	Yes	No	Yes	Yes	No
	Blazar						
		FSRQ	No	Yes	Yes	Some	Yes
		BL Lacs	No	No	No	No	Yes
RQ							
	Seyfert 1		$< 10\%$	Yes	Yes	Yes	No
	Seyfert 1.5		$\sim 30\%$	Yes	Yes	Yes	No
	Seyfert 2		$> 90\%$	No	Yes	Yes	No
	ULIRGs		Yes	Yes	Yes	No	No
	LINER		Yes	No	Yes	Yes	No

Table 1.1.: Overview over the properties of different types of AGN, adapted from Beckmann and Shrader, 2012

lobe emission from the originating galaxy. FSRQs are also associated with Blazars which alongside the BL Lac objects are the objects where the observers line of sight is closest to the jet axis. The implications of this will be more detailed discussed in the next section. Blazars share the features common with the Quasars but show additional narrow line features in their spectra. A table of all the different properties and characteristics of the AGN is given in Tab.1.1.

1.1.2. Unification Model

As shown above there are a lot of different properties and characteristics joint under the big class of AGN, so one has to ask the question what keeps them connected. There were some early attempts to connect the pieces together like Weedman (1973) or Antonucci (1993). Later Urry and Padovani (1995) did a more detailed analysis on how the connection could be achieved by proposing a model which relies on the line of sight to the object but keeps the basic structure overall.

The central feature is the bright luminosity of the objects, which can be expressed through the bolometric luminosities of AGN reaching from $L_{bol} = 10^{41}$erg s^{-1} to $L_{\rm bol} = 10^{48}$erg s^{-1}. These luminosities indicate that they stem from accretion of a central mass as shown in King (2008). The maximal luminosity which can be produced from the

accretion is the Eddington luminosity which can be derived from the accretion rate of spherical symmetrical accretion into a black hole

$$\dot{M} = \frac{4\pi\rho G^2 M_{\mathrm{BH}}^2}{V^3} \qquad (1.1.2)$$

with ρ giving the density of the accretion flow, M_{BH9} the mass of the black hole and V the Volume of the black hole. This rate, as pointed out by Eddington, is limited by the mass of the compact object M and it is assumed to accrete ionized hydrogen thus leaving us with the Eddington-luminosity

$$L_{Edd} = \frac{4\pi G M m_{\mathrm{p}} c}{\sigma_{\mathrm{T}}} \simeq 1.3 \times 10^{38} \frac{M}{M_{\odot}} \mathrm{erg\,s}^{-1} \qquad (1.1.3)$$

with m_{p} the proton mass and $\sigma_T \simeq 6.65 \times 10^{-25} cm^{-2}$ the Thomson scattering cross section.

If we compare the mass necessary to achieve the luminosities in AGN to the mass of the sun $M_{\odot}$ the result of the central masses yields $M \sim 10^5 M_{\odot}$ up to $10^{10} M_{\odot}$. The black holes have therefore a very high mass and span a new category called super-massive black-holes (SMBH). They are surrounded by an accretion disc of hot plasma fuelling the accretion process of the SMBH. The accretion discs have radii of r 10^{-3}pc and are surrounded by an optical thick dust torus located at a distance of around r 10^1pc up to 10pc from the SMBH. The previously mentioned broad emission line features in some of the AGN originate in a region close to the core region, where photonized gas is moving in rapid clouds, leading to line widths of 10^3kms^{-1} up to 10^{-4}kms^{-1}. According to the emission line features, the region is called the broad-line region(BLR). It is surrounded by the opaque dust torus and for higher viewing angles the BLR becomes invisible. The narrow line region(NLR) is located further away of the central SMBH and consists of colder and less dense accumulated gas clouds compared to the BLR. These gas clouds produce the narrow features in the spectrum at line widths of 400kms^{-1} to 500kms^{-1} an overview over the basic pieces with some properties can be found in Table 1.2. A scheme how the physical properties of the different morphologies compare, can be found in Table1.1 in Section 1.1.1. A graphical depiction of the unification model is shown in Fig.1.1.

1.1.3. Radiation Processes in AGN

In the previous section it was mentioned that AGN emit radiation over the full electromagnetic spectrum. This section will shed some light on how the spectrum of a typical AGN will look like and what the main processes behind this profile are. The explanations of the radiation processes are based on Beckmann and Shrader (2012). As shown in Fig. 1.2 the characteristic profile of an AGN is the "double-hump" structure. The example MRK 421 is a blazar where due to beaming the most fundamental processes dominate. If then the inclination gets increased, additional features will become visible,

-	Radius R	Density n in cm^{-3}	velocity v
Inner accretion disc radius	$0.01 - 60$ AU	10^{15}	0.3 c
Outer accretion disc radius	$1 - 1000$ AU	-	-
Dust torus	$1 - 10$ pc	$10^3 - 10^6$	-
BLR	$0.01 - 1$ pc	10^{10}	$1000 - 5000$kms^{-1}
NLR	$100 - 10000$ pc	$10^3 - 10^6$	few 100kms^{-1}
Jet	Up to 100 kpc	-	$0 - 40$ c

Table 1.2.: Overview over the essential pieces of an AGN after the unification model. Adapted from the lecture of Kadler, 2015 with some details added from Beckmann and Shrader, 2012
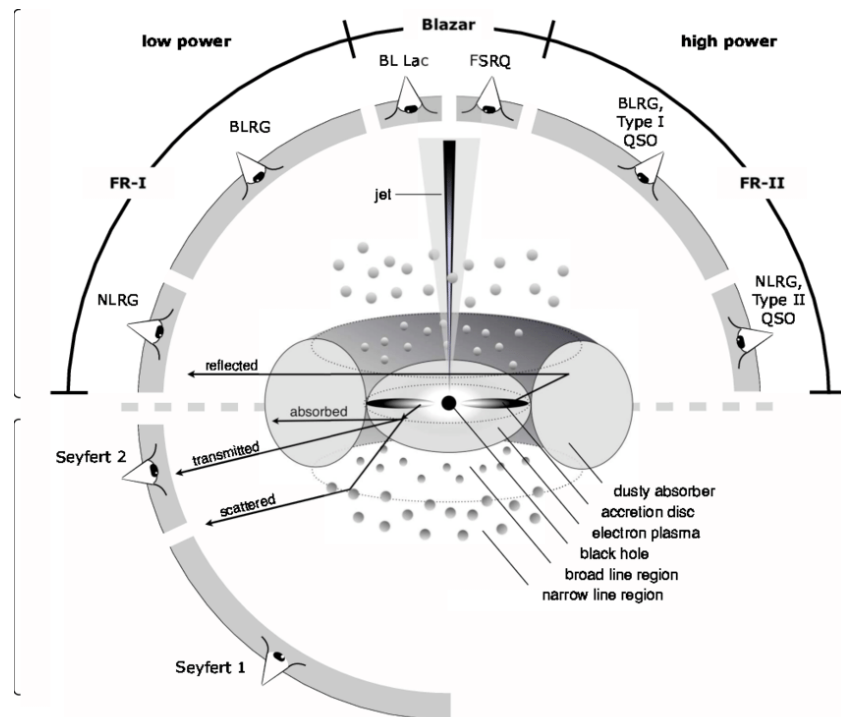
Figure 1.1.: Depiction of the underlying principle of the unification model. All the different sub-types are connected by the different angle between the observer and the object. The lower half shows a radio-quiet AGN, the upper one the radio-loud ones. For simplicity both different categories of objects are compressed in one scheme.
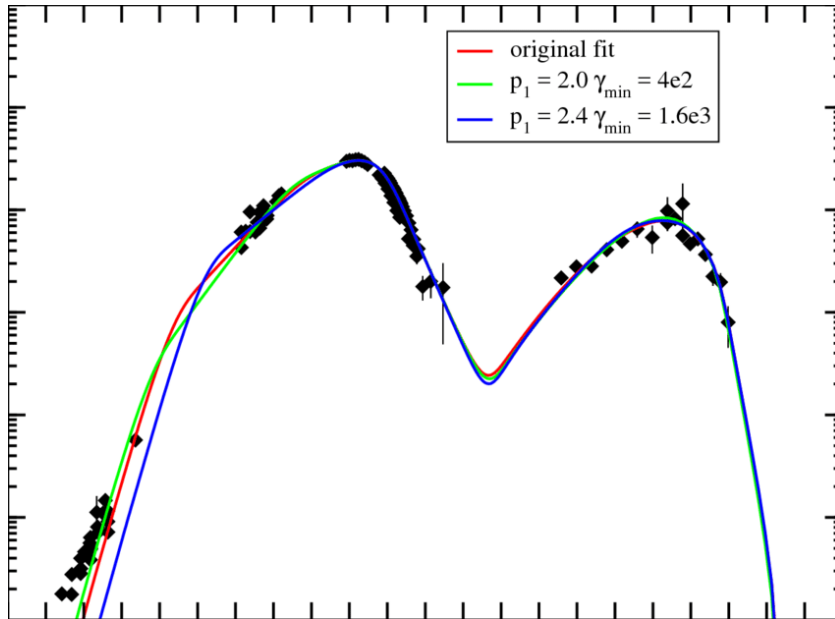
Figure 1.2.: Typical radiation structure of an AGN, shown by the characteristic "double hump" structure in the AGN Mrk 421, adapted from Aleksic, m.-w. p. m.-w., and Moody (2011)

which can be seen in the X-ray regime. The lower hump in the radio regime is caused by synchrotron emission, the upper one is still debated and is caused either by inverse Compton scattering (e.g as proposed by Blandford and Königl (1979)), (Konigl, 1981) or as it is shown by Mannheim (1993) it is produced by pion decay into photons and neutrinos. Additional X-ray components are caused by absorption and reflection effects resulting out of Thomson scattering.

Synchrotron Radiation

Synchrotron emission occurs when a charged particle is accelerated or deflected in a magnetic field. A charged particle with the charge $q = Ze$, the rest mass m and a Lorentz factor of

$$\gamma = \frac{1}{\sqrt{1 - v^2/c^2}} \tag{1.1.4}$$

is travelling through a uniform and static magnetic field, with the velocity vector of $\vec{v}$. The Lorentz force on said charged particle is then given by

$$\frac{\mathrm{d}}{\mathrm{d}t}(\gamma\, m\, \vec{v}) = \frac{Ze}{c}(\vec{v} \times \vec{B}). \tag{1.1.5}$$

The acceleration is perpendicular to the trajectory of the particle, so the velocity v and

therefore the Lorentz factor γ are constant. Moreover the force is perpendicular to the direction of the magnetic field and therefore the velocity component along the magnetic field lines $v_\parallel$ is constant. Since the overall velocity and the velocity component along the field lines are constant the velocity perpendicular to the field lines $v_\perp = \sqrt{v^2 - v_\parallel^2}$ should be as well with a changing direction. Since the force is shifted in a right angle to the velocity, the particle will perform a circular movement perpendicular to the magnetic field or a helical movement overall. The gyration frequency of the particle is called the Larmorfrequency and is given by

$$\omega_L = \frac{ZeB}{\gamma mc}. \tag{1.1.6}$$

The resulting luminosity of the acceleration is then expressed by

$$L = \frac{2Z^2 e^2}{3c^3} \gamma^4 \left[\left(\frac{\mathrm{d}v_\perp}{\mathrm{d}t} \right)^2 + \gamma^2 \left(\frac{\mathrm{d}v_\parallel}{\mathrm{d}t} \right)^2 \right]. \tag{1.1.7}$$

There is no acceleration perpendicular to the velocity so $\mathrm{d}v_\parallel/\mathrm{d}t = 0$. For the circular trajectory of the particle the acceleration is $\mathrm{d}v_\perp/\mathrm{d}t = \omega_l v_\perp$. The perpendicular velocity can be expressed through the total velocity and the pitch angle β between the trajectory of the particle and the magnetic field $v_\perp = v \sin \beta$. If we combine it with the luminosity it yields

$$L = \frac{2Z^4 e^4 B^2 \gamma^2 v^2 \sin^2 \beta}{3c^5 m^2}. \tag{1.1.8}$$

Since the mass is influencing the luminosity by $L \propto m^{-2}$, only light particles will have a relevant impact and therefore only electrons and positrons will be considered. This implies that in the following the elementary charge e will replace our general charge q.

Another factor influencing our received synchrotron radiation is that so far we only considered isotropical radiation profile. Because of the relativistic properties beaming effects can occur and should therefore be considered. The particles velocity vector will be concentrated in a narrow cone with an opening angle of $\Phi \simeq \gamma^{-1}$. As the particle is moving helical along the field lines, the observer only will detect emission when the cone is directed towards him, similar to the effect of a lighthouse. Therefore, the observer will only receive pulses of emission with a smaller width than ω_g. As shown in Rybicki and Lightmann (1985) one can derive the resulting spectrum from the single particles, which have a maximum at the critical velocity $v = 0.29\,v_\mathrm{c}$. The spectrum itself scales with the energy of the particles with $v_\mathrm{c} \propto E^2 \propto \gamma^2$. For the derivation of the power, dependant on the observed frequency band, we yield

$$L(E, \nu) = \frac{\sqrt{3} Z^3 e^3 B \sin \beta}{mc^2} F(x), \tag{1.1.9}$$

where x is a function of the velocities with $x = v/v_\mathrm{c}$ or more explicit, depends on the modified Bessel-function $K_{5/3}$,

$$F(x) = \frac{v}{v_\mathrm{c}} \int_{v/v_\mathrm{c}}^{\infty} K_{5/3}(\zeta)\mathrm{d}\zeta. \tag{1.1.10}$$

So far only one particle was considered but astronomical sources usually persist out of particle ensembles in form of plasma. With consideration of the previous assumptions we can state for the luminosity of such a plasma

$$L(\nu) = \int_{E1}^{E2} L(E, \nu)n(E)\mathrm{d}E. \tag{1.1.11}$$

n describes the density of electrons in an energy interval of $E + \mathrm{d}E$, which is taking the form of a power law $n(E) = \mathrm{d}E = kE^{-p}\mathrm{d}E$. The normalization k and the power law index p are both constant so that means basically for the scaling of the luminosity

$$L(\nu) \propto \nu^{-\alpha}. \tag{1.1.12}$$

α can be identified as spectral index in the form of $\alpha = \frac{p-1}{2}$.

Another consideration is that this calculation only holds in optically thin media, since the optical depth τ_ν of a medium for a passing through photon is defined by

$$\tau_\nu(s) = \int_{so}^{s} \kappa_\nu(s')\mathrm{d}s'. \tag{1.1.13}$$

κ_ν is the absorption coefficient, meaning that if $\tau_\nu > 1$ the medium is optically thick. The other case $\tau_\nu < 1$ shows that the medium is optically thin. In optically thick media the photons of the lower energies act with the electrons of the medium itself and get absorbed, hence the effect is called synchrotron self-absorption. The spectrum changes in proportion so the flux density is

$$S(\nu) \propto \nu^{5/2}. \tag{1.1.14}$$

The optically thick medium dominates the spectrum only under a certain frequency ν_sa where the medium becomes transparent again and the flux density changes to the form above

$$S(\nu) \propto \nu^{\frac{p-1}{2}}. \tag{1.1.15}$$

Inverse Compton Scattering

In the process of Compton scattering the photon transfers energy to an electron. In relativistically moving material the opposite of this effect can happen. Low energetic photons can scatter up on the relativistic electrons and gain very high energies this way because of the highly differing mass compared to the electrons. This is called the inverse

Compton scattering. For better understanding we start in the laboratory frame with a scattering event L. The frame of the relativistic electron L' then depends on the Lorentz factor γ and the energy of the photon in L' is determined by

$$h\nu' = \gamma h\nu \left(1 + \frac{v_{\mathrm{e}}}{c}\cos\Theta\right), \tag{1.1.16}$$

where h is considered as Planck's quantum of action, v_{e} is the velocity of the electron and ν / ν' are the frequencies of the electrons in the belonging frame. θ is the angle between the direction of the photon and the electron in the laboratory frame, since in the relativistic frame the angle would seem smaller. The photon energy in comparison to the rest energy of the electron is very small so we can treat the scattering as an elastic process. This means that the energy of the photon in the electron frame is conserved to $E_2' \simeq E_1'$ for the energy E_1 before the scattering and E_2 after the scattering event. If we convert it back to the laboratory frame we get for the photon energy

$$E_2 \simeq \gamma^2 E_1. \tag{1.1.17}$$

Therefore, the photon gains in the scattering energy proportional to γ^2. Due to constraints of energy conservation this is limited to $E_2 \leq E_1 + \gamma m_{\mathrm{e}} c^2$ which means for the maximum change of photon frequency $\Delta\nu$

$$\Delta\nu \leq \gamma m_{\mathrm{e}} c^2 h^{-1}. \tag{1.1.18}$$

The power or the luminosity depends on the density of the photons n_{ph} which is tied directly to the energy density of the electron field U_{ph}

$$L_{\mathrm{IC}} \propto n_{\mathrm{ph}}\gamma^2 E_1 \propto \gamma^2 U_{\mathrm{ph}}. \tag{1.1.19}$$

The photons used for the IC process can originate in the medium itself by synchrotron emission, hence the process is called synchrotron self-Compton (SSC). This only works if the plasma is optically thick. The luminosity of the IC process does not depend on the energy density of the photon field but on the density of the magnetic field. Since the effect can power itself, the effect is very sensitive to the brightness of the source, because above a certain brightness temperature T_b the process efficiently cools down the electrons. The threshold of this brightness temperature is around $T_b \sim 10^1 2K$, since then the effect of synchrotron self absorption dominates it. For the luminosity ratio of the involved processes this means

$$\frac{L_C}{L_S} \sim \frac{1}{2}\left(\frac{T_b}{10^{12}K}\right)^5 \left[1 + \frac{1}{2}\left(\frac{T_{max}}{10^{12}K}\right)^5\right]. \tag{1.1.20}$$

When $T_{\mathrm{b}} > T_{\mathrm{tresh}}$ the inverse Compton eradicates the synchrotron emission, which is an effect called inverse Compton catastrophe. There is to mention that in some cases of low inclinations the limit can be exceeded by boosting effects up to $T_{\mathrm{b}} = 10^{13}\,\mathrm{K}$ such as

found by Wehrle et al. (2001).

Hadronic Emission

Another possibility of the high energy emission hump is is not caused by leptonic models, but by hadronic ones. If the energy of a photon exceeds the sum or rest mass of a particle and its corresponding anti-particle this leads to pair production. The most common pair production would be of those of an electron and an positron. There is also relativistic material present which enhances further interaction like photon-proton interaction. Since energy is available in the medium and also high magnetic fields are present different particle cascades can develop. This has been proposed by Mannheim (1993) or Boettcher (2010), which describe their model through pion production. Those will cascade down if a threshold is exceeded assisted by the synchrotron radiation. The possible decay process to produce the received emission can be π^0-decay, electrons from a charged pion decay $\pi^{\pm} \rightarrow \mu^{\pm} \rightarrow e^{\pm}$, p-synchrotron and μ-, π- and K-synchrotron photons.

Accretion Disc Reflection and Absorption

So far only the continuum of the X-ray spectrum has been covered, while this holds for Blazars or sources with high inclination, where beaming effects dominate, for lower inclinations other effects become visible. The following explanations summarize the explanations of Turner and Miller (2009). Taking into account that the accretion disc consists out of mass, it can interact with on-falling and passing through radiation, which transmit into absorbed spectral shapes. This is shown especially between the $0.1 - 10 \text{keV}$ band, where X-ray photons can excite and ionize electrons in carbon and nickel atoms. The ionization in the photoionized gas can be expressed by the ionization parameter ξ, which compares the ionizing luminosity to the density of protons n

$$\xi = \frac{L}{nr^2}. \tag{1.1.21}$$

Out of convention this parameter is often compared to the column density of hydrogen atoms N_{H}, using solar Abundances. The Absorption is dominated by heavier atoms and hydrogen has very insignificant impact. Absorbing gas also is producing line emission, which can be seen at 6.4keV. This is caused by relaxation of K-shell electrons into lower energy states, which produces a Kα Photon in the process. The mentioned energy line is more specific associated with iron, which has always high abundances as the most stable fusion element. The luminosity of those fluorescence lines is given by

$$L_{\mathrm{K}\alpha} = \frac{E_{\mathrm{K}\alpha}}{2 + \Gamma} \langle Y \rangle \frac{\Delta\Omega}{4\pi} L_0 \langle \tau_0 \rangle, \tag{1.1.22}$$

with Γ as the photon index of the continuum and $E_{\mathrm{K}\alpha}$ as the energy of the emission

line. Further is $\langle Y \rangle$ the fluorescence yield averaged over the ionized states and $\langle \tau_0 \rangle$ is the optical depth.

For high column densities Compton scattering take place, which leads to reflection. For X-ray photons $h\nu = m_c^2$, which means we can approximate the Compton scattering cross-section with the Thompson cross-section. If solar abundances is assumed for the material, Compton scattering and photoelectric absorption equals at around $10 \, \mathrm{keV}$, making this the lower threshold to introduce Compton reflection components. This leads to an hump in the spectral shape with its maximum at around $\gtrsim 30 \, \mathrm{keV}$, since then the reflection is reaching the maximum. The explanations for the Thompson cross-section follow after Beckmann and Shrader (2012). The electron radius $r_0 = q^2/(mc^2)$ leads to an differential cross-section of

$$\frac{d\sigma}{d\Omega} = \frac{1}{2}(1 + \cos^2 \theta) r_0^2 \tag{1.1.23}$$

This process is symmetric regarding the angle and thus the total cross-section yields

$$\sigma_{\mathrm{T}} = 2\pi \int_0^\pi \sin\theta d\theta = \frac{8\pi}{3} \left(\frac{q^2}{mc^2} \right)^2 \tag{1.1.24}$$

The chance that a photon is scattered at an proton is connected to the density expressed through the optical depth τ

$$\tau = \int \sigma_{\mathrm{T}} n_{\mathrm{p}} dx \tag{1.1.25}$$

The cross-section for a photon scattering at Protons is $\sigma_{\mathrm{T}} \simeq 1.95 \cdot 10^{-31}$ and hence the large densities are needed.

1.1.4. Jet Physics

Almost all of the radio emission is produced in the radio jets as mentioned earlier in Section 1.1.1. In order to analyse the behaviour in the radio regime it is of importance to understand first what they consist of and how they shape the radiation received by an observer. This section will mention first the morphology and structure of the jets, then shed some light at the effect of apparent superluminal motion and end with a discussion on beaming effects and the Doppler boosting of the jets. The references for this section rely on Beckmann and Shrader (2012) and the paper of A. P. Marscher (2009), if not mentioned otherwise.

Jet Morphology

Jets are extremely energetic and highly collimated plasma structures that form in the inner parts of the AGN and flow outwards. They can reach out to hundreds of kilo parsecs or even further. The acceleration process is not fully clear yet, especially in the

vicinity of the black hole, but some debate that the accretion disc is connected to the jet like A. Marscher et al. (2002). The most common presumption relies on the work of (Blandford and Znajek, 1977) which assumes energy extraction from the black hole. For this to work, a spinning black hole is needed, since this influences the magnetic field lines near the accretion disc. The reconfiguration and tightening of the field lines launches the plasma outwards, a bit like a geyser. The explanations of the jet physics in general lie in the field of magnetohydrodynamics(MHD). It is not quite clear where the acceleration of the jet to the high bulk Lorentz factors happens, since the high energy density would lead to very high Compton scattering and a substantial energy loss so it is believed that most of the acceleration takes place further away.

In the radio regime the velocity of the jet can be measured by features in the jet, which are localized intensities caused by shocks in the jet plasma. Relativistic fluid velocities exceed the local sound speed and form knots near the central engine. Electrons are accelerated in the shock front and then losing the energy again in the radiation process. The plasma expands transversal behind the shock front leading to a stratification of the energy density with the peak exactly behind the shock front. These shock fronts are often called "blobs" will then propagate outwards along the jet flow and expand in the process, reducing their luminosity. They are often case of radio studies because of their movement, which depends on the source. They can be superluminal, subluminal moving or just staying stationary. A schematic depiction of a radio jet in a quasar is shown in Fig.1.3 with the different radiation regions in the lower part of the picture.

Superluminal Motion

A effect seen in several radio jets is superluminal motion, where the features in the jet move apparently faster than the speed of light. In general the maximal speed achievable in the speed of light so one has to ask the question how it is possible that jet knots achieve those superluminal speeds. In the following this effect gets debunked as a harmless projection effect.

Consider a jet component moving towards the observer at a relativistic speed v inside the jet under an angle ϕ to the line of sight. The component emits a first signal at the time t_0 and at a later time $t_1 = t_0 + \Delta t$ as depicted in Fig. 1.4. For the observer the signals arrive at modified times through the different distances the photon needs to travel, so $t_0' = t_0 + \frac{s_1 + s_2}{c}$ and $t_1' = t_1 + \frac{s_2}{c}$. As shown in the sketch s_1 and s_2 are the corresponding distances. Between the emission of the two signals the component moves the distance $s_1 = v\Delta t_{\text{signal}} \cos\phi$ towards the observer. The time between the observation of the signals can be calculated by

$$\Delta t_{\text{obs}} = t_1' - t_0' = \Delta t_{\text{emit}} - \frac{s_1}{c} = \left(1 - \frac{v}{c}\cos\phi\right)\Delta t_{\text{emit}}. \qquad (1.1.26)$$

To calculate the apparent velocity, the apparent travel distance Δx_{app} is necessary by $\Delta x_{\text{app}} = v\Delta t_{\text{emit}} \sin\phi$, leading to
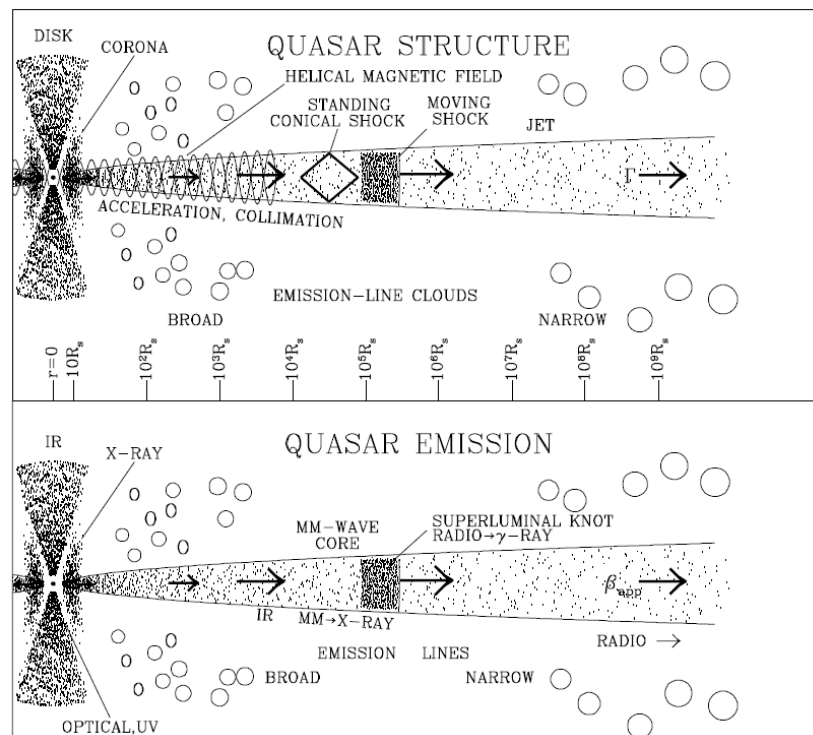
Figure 1.3.: Schematic depiction of a disc-jet structure. The intensity of the emission is highlighted by the density of the dots. Also the different emission regions are shown. Adapted from A. P. Marscher, 2009.
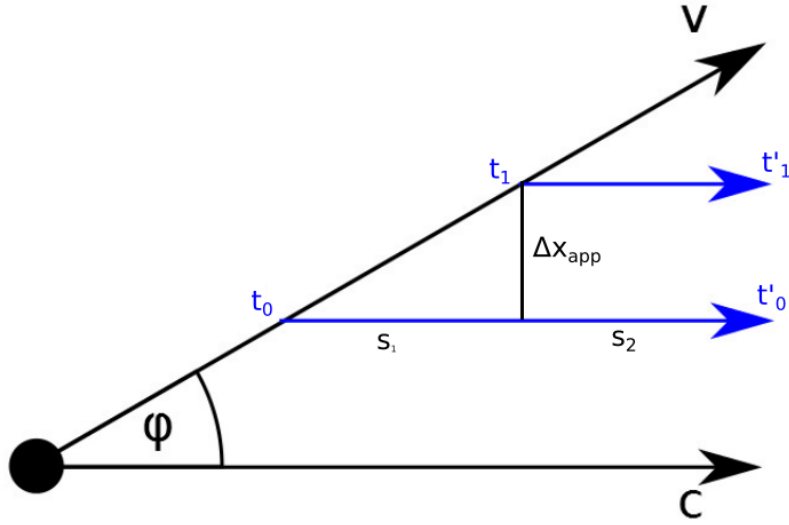
Figure 1.4.: Sketch of a jet component emitting a signal at two different times t_0 and t_1 through the travel times of the photons the signal arrives at the observer at the times t'_0 and t'_1

$$\frac{v_{\text{app}}}{c} = \frac{\Delta x_{\text{app}}}{c \Delta t_{\text{obs}}} = \frac{v \sin \phi}{c(1 - v/c \cos \phi)}. \tag{1.1.27}$$

Alternatively, the equation can be expressed in terms of the speed of light $\beta = v/c$, thus

$$\beta_{app} = \frac{\beta \sin \phi}{1 - \beta \cos \phi}. \tag{1.1.28}$$

This will later be used to determine the inclination angle, the angle to the line of sight, for 2043+749.

Beaming

Jets in AGN are considered to be symmetrical in flux which is a case rarely achieved in observation. The cause of this deviation lies in the beaming of the jet towards the observer and a lessening of the flux in the opposite direction. The Doppler Factor D is given by

$$D = \frac{1}{\gamma (1 - \beta \cos \phi)}. \tag{1.1.29}$$

For the intensity of the radiation, it can be shown, as done in Rybicki and Lightmann

(1985), that $I(\nu)/\nu^3$ is Lorentz invariant. For the received luminosity this means that

$$L(\nu_{\mathrm{obs}}) = D^p L(\nu_{\mathrm{emit}}) \tag{1.1.30}$$

where p depends on which luminosity is observed. If the luminosity is measured over the whole jet $p = 2 + \alpha$, whereas if the luminosity is measured for a single component it yields $p = 3 + \alpha$. Since this happens in both directions, the ratio R of the jet flux density F_{Jet} and the counter jet flux density F_{CJ} yields

$$R = \frac{F_{\mathrm{Jet}}}{F_{\mathrm{CJ}}} = \left(\frac{1 + \beta \cos \phi}{1 - \beta \cos \phi} \right), \tag{1.1.31}$$

which will also be used to calculate the inclination later on.

1.2. Radio Observations and VLBI

The Atmosphere of the Earth plays a major role in the study of astronomical objects. While the effects in the radio and optical regime are very minor in the higher energy regimes like X-ray and γ-ray the atmosphere is almost opaque. Since there is a window in the radio regime we can observe with ground based telescopes but due to the Rayleigh-criterion

$$\Theta \approx 1.22 \frac{\lambda}{D} \tag{1.2.1}$$

this brings some problems as well. Θ gives us the resolution limit in radians for a given wavelength λ and diameter of the observing telescope D. This means that for our largest operating radio telescopes it is not possible to resolve the innermost structures of the AGN. Therefore the solution would be to use a procedure called very-long-baseline interferometry or in the following abbreviated VLBI. The technique uses an array of radio telescopes and through correlating the data together the resolution limit is given by the largest baseline between the telescopes. An introduction into VLBI will be given in the next section, which if not stated otherwise, uses the textbook of Burke and Graham-Smith (2009) and Thompson and Swenson Jr. (2017) as references.

1.2.1. Single Dish Observation

Incoming radiation of the universe can be treated as a superposition of electro-magnetic waves, which especially in the radio regime carries a lot of noise. At higher energy it then gets dominated by discrete photons but for the radio regime it can be treated as random Gaussian noise. Consider a flux S emitted by a source and received in our radio telescope. Since this flux depends on a frequency ν and is measured over a finite receiving band, an auxiliary concept of flux per frequency or flux density S_ν is necessary

$$S = \int S_\nu \mathrm{d}\nu. \tag{1.2.2}$$

A useful tool to measure the flux density of a source is to compare it to the brightness temperature of a black body at a physical temperature T_b linking them to

$$S_\nu = 2kT_\mathrm{b}\Omega_\mathrm{source}/\lambda^2. \tag{1.2.3}$$

In this equation k is the Boltzmann factor and Ω_source is a solid angle on the source. The source angle compared to the reception angle of the beam is then defining the temperature received in the antenna T_a of our telescope

$$T_\mathrm{a} = T_\mathrm{source}\frac{\Omega_\mathrm{source}}{\Omega_\mathrm{a}}, \tag{1.2.4}$$

with T_source is the temperature in the source. Since the sources usually observed in the radio are very far away, the antenna beam will be larger than the source angle and the antenna temperature can be rewritten as a dependency of the effective area of the telescope

$$T_\mathrm{a} = \frac{S_\nu A_\mathrm{eff}}{2k}. \tag{1.2.5}$$

The effective area of the telescope depends on the angle of the telescope to the source and is defined by its antenna beam pattern. The brightness of the source is collected by the main lobe as depicted in Fig. 1.5a, while the side lobes contribute noise. Therefore, the effect of the side-lobes should be minimized which scales with the size of the telescope.

1.2.2. Two-Element Interferometer

The easiest start to describe the principles of VLBI is to start with the easiest interferometer, the two-element interferometer. This is an array consisting out of two identical telescopes separated by a baseline b, which observe the same physical source. A sketch of the experimental construction is given in Fig. 1.9. The signal reaches the second antenna with a time delay $\tau_\mathrm{g} = b \cdot s/c$. The cross-spectrum power density of both signals can be achieved by a Fourier transformation of the cross-correlation $R_\mathrm{xy}(\tau)$ with the convolution theorem. This means that the transformation of $x(t)$ is multiplied with the complex conjugated transformation of $y(t)$ to

$$S_{xy}(\nu) = X(\nu)Y^*(\nu). \tag{1.2.6}$$

A monochromatic signal is for $y(t)$ shifted through the time delay, this translates in a time delayed signal $y(t - \tau_\mathrm{g})$ and transforms in a phase shifted delta peak of $2\pi\nu\tau_\mathrm{g}$. The result for the flux density yields
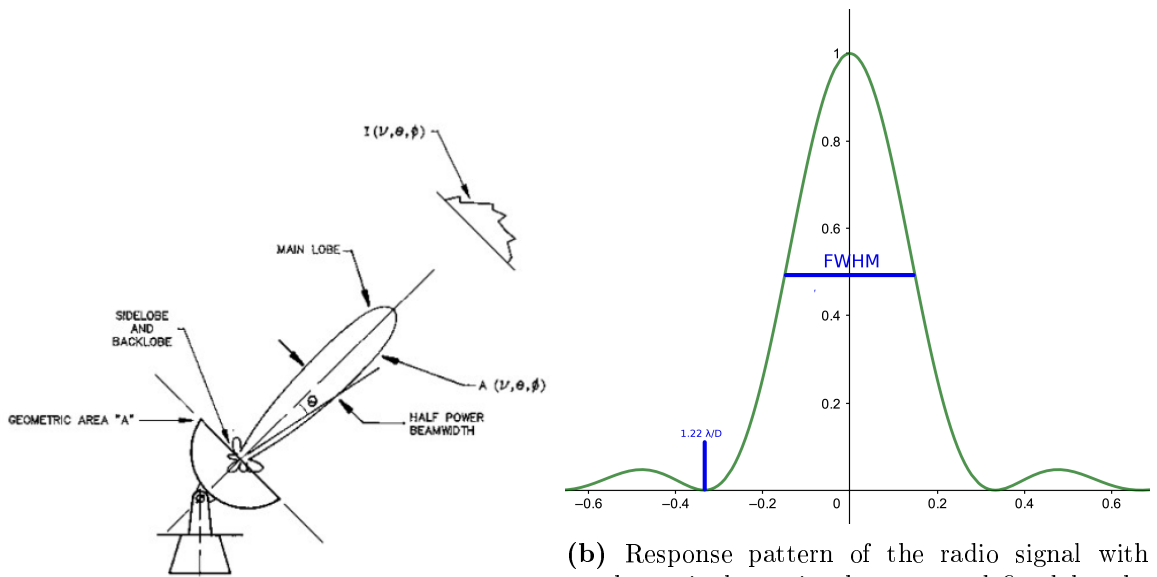
(a) Schematic of the reception of a radio antenna adapted from (Bach, n.d.).

(b) Response pattern of the radio signal with the main beam in the center, defined by the full-width-half-maximum(FWHM) and development of side lobes.
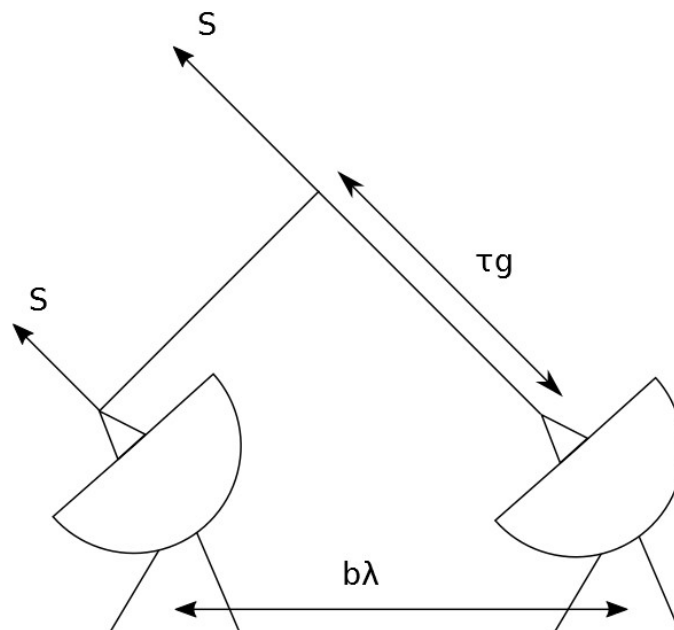
Figure 1.6.: Schematic of an easy interferometer with two radio dishes. Both are placed a distance b away given in the wavelength λ and receive the same source signal S. The time delay between the Signals can be measured by τ_{g}.

$$S_{\text{XY}}(\nu) = A(\vec{s})S \exp(\text{i}2\pi\vec{b_\lambda} \cdot \vec{s}) \tag{1.2.7}$$

where $\vec{b_\lambda} = \vec{b}/\lambda$ contains a dependency on the observed wavelength. Since the observed signals are not monochromatic in nature, but emit over a continuum, the interferometers operate with finite bandwidths which has to be taken into account. This can be realised by a square bandpass centered on ν_0, which spans the bandwidth $\Delta\nu$ and becomes 0 beyond the borders. Based on the assumptions that the flux density remains constant and the effective area can be treated as such the flux density can be transformed to

$$S_{\text{XY}}(\vec{s}) = \mathcal{A}(\nu_0, \vec{s})S(\nu_0)\text{sinc}[\Delta\nu(\tau_{\text{g}} - \tau_{\text{i}})] \exp[-2\pi\nu_0(\tau_{\text{g}} - \tau_{\text{i}})] \tag{1.2.8}$$

The antenna area gets modified to the relative antenna area $\mathcal{A}$ carrying the delay beam term in it and is normed to the direction $\vec{s_0}$. In the expression a second oscillation term appears $\exp[-2\pi\nu_0(\tau_{\text{g}} - \tau_{\text{i}})]$, which describes fringe oscillations. This term recedes if the delay beam term $\text{sinc}[\Delta\nu(\tau_{\text{g}} - \tau_{\text{i}})]$ gets dominant due to a very small time delay. The above assumptions for the band pass can have an effect and should be considered in high precision measurements.

So far, the calculations only hold for point sources. Therefore, the next step is to extend the model to finite sources which are characterized by brightness distributions $B(\theta)$ instead of flux densities. A directional vector $\vec{s_0}$ is therefore introduced which points at the center of the source. A position relative to the source center than can be given by $\vec{\delta}$ thus $\vec{s} = \vec{s_0} + \vec{\delta}$ as depicted in Fig. 1.7.

The cross-spectrum power density can then be gained by integration over the whole radio source

$$S_{\text{xy}}(\vec{s_0}) = \int \mathcal{A}(\vec{\delta})B_\nu(\vec{\delta}) \exp\{-i2\pi[\vec{b_\lambda} \cdot (\vec{s_0} + \vec{\delta}) - \nu\tau_{\text{i}}]\}\text{d}\Omega. \tag{1.2.9}$$

For this to work, the source has to be smaller than the response pattern of the delay beam so the effects can be neglected. Another result of this assumption is that ν_0 can be treated as the defining frequency for the band pass. The geometrical phase term can be compensated with an instrumental delay, thus simplifying the equation

$$V(\vec{b_\lambda}) = \int \mathcal{A}(\vec{\delta})B_\nu(\vec{\delta}) \exp(-i2\pi\vec{b_\lambda} \cdot \vec{\delta})\text{d}\Omega, \tag{1.2.10}$$

which gives a relation for complex visibility $V(\vec{b_\lambda})$. This is the fundamental equation for a practical interferometer. As already teased in Fig. 1.7 it is useful to introduce a new coordinate system perpendicular to the source direction, which uses conventionally (u, v, w)-coordinates. The (u, v)-plane is the considered the projectional plane of $\vec{\sigma}$, while the w coordinate is parallel to $\vec{s_0}$. Since w is perpendicular to the (u, v)-plane it can be set to 0. The indices (l, m, n) relate to the components of a unit vector in the direction of $\vec{s}$. The element of the solid angle $\text{d}\Omega$ projects along the direction $\vec{s}$ an element of the
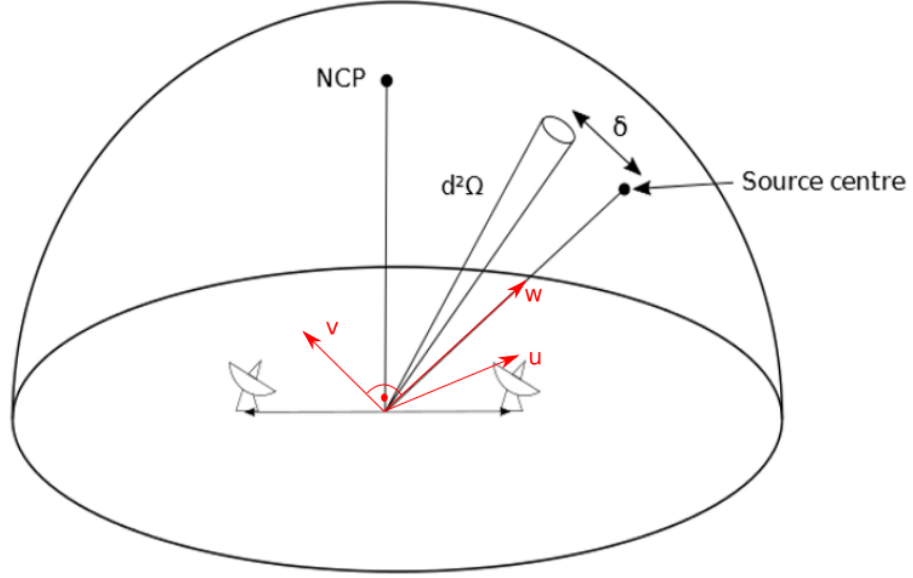
Figure 1.7.: Setup for the two element interferometer with the pointing towards an extended source. The (u,v) plane maps the position of the telescopes relative to the source center.

area $\mathrm{d}l\mathrm{d}m$ in the (l, m)-plane and thus

$$\mathrm{d}\Omega = \frac{\mathrm{d}l\mathrm{d}m}{\cos\gamma} = \frac{\mathrm{d}l\mathrm{d}m}{\sqrt{1-l^2-m^2}}, \tag{1.2.11}$$

where γ spans an angle between $\vec{s_0}$ and $\vec{s}$. If Eq.1.2.10 gets transformed with the new coordinate system it yields for the visibility

$$V(u,v) = \int\int \mathcal{A}(l,m)B_\nu(l,m)\exp(-\mathrm{i}2\pi(ul+vm))\frac{\mathrm{d}l\mathrm{d}m}{\sqrt{1-l^2-m^2}} \tag{1.2.12}$$

$V(u,v)$ is now a 2D Fourier-transformation of the modified source brightness

$$V(u,v) \overset{\mathcal{F}}{\longleftrightarrow} \frac{\mathcal{A}(l,m)B_\nu(l,m)}{\sqrt{1-l^2-m^2}} \tag{1.2.13}$$

Commonly, the observed sources are very far away compared to the size of the source meaning σ is very small. This implies that the cartesian coordinates x and y are parallel to u and v. Furthermore, small angle approximation can be applied and the antenna beam size is large compared to the field of view. Taking this into account the visibility can approximated by

$$V(u, v) \approx \int B(x, y) \exp[-\mathrm{i}2\pi(ux + vy)]\mathrm{d}x\mathrm{d}y, \tag{1.2.14}$$

or

$$V(u, v) \underset{\mathcal{F}}{\longleftrightarrow} B(x, y). \tag{1.2.15}$$

In conclusion can the complex visibility function be inversely Fourier transformed into the brightness distribution.

1.2.3. VLBI

In the previous section it was described how two telescopes can be linked together via a Fourier-transformation to an interferometer. This can be used to expand the array with further telescopes to get $N(N-1)/2$ baselines to improve the visibility, with N is the amount of elements in the array. These explanations follow T. Cornwell and B. (1999). The observed visibility $\tilde{V}_{\mathrm{ij}}$ for the i-j baseline and the actual visibility are linked via

$$\tilde{V}_{\mathrm{ij}}(t) = g_{\mathrm{i}} g_{\mathrm{j}}^* V_{\mathrm{ij}} \tag{1.2.16}$$

where g_{i} and g_{j} are the gain factors the elements i and j. The phase part of the visibility transforms to

$$\tilde{\Phi}_{\mathrm{ij}} = \Phi_{\mathrm{ij}} + \theta_{\mathrm{i}} - \theta_{\mathrm{j}}, \tag{1.2.17}$$

in which θ_{i} and θ_{j} represent small errors in the phase. If a loop out of three elements i,j and k is formed, then the observed closure phase $\tilde{C}_{\mathrm{ijk}}$ is given by

$$\tilde{C}_{\mathrm{ijk}} = \tilde{\Phi}_{\mathrm{ij}} + \tilde{\Phi}_{\mathrm{jk}} + \tilde{\Phi}_{\mathrm{ki}} =$$
$$\Phi_{\mathrm{ij}} + \theta_i - \theta_j + \Phi_{\mathrm{jk}} + \theta_j - \theta_k + \Phi_{\mathrm{ki}} + \theta_k - \theta_i =$$
$$\Phi_{\mathrm{ij}} + \Phi_{\mathrm{jk}} + \Phi_{\mathrm{ki}} = C_{\mathrm{ijk}}.$$

So, the closure phase is a good observable, since it is independent from the phase errors of the telescopes. In the same fashion a closure amplitude can be derived for any loop of at least four elements

$$\Gamma_{\mathrm{ijkl}} = \frac{|\tilde{V}_{\mathrm{ij}}||\tilde{V}_{\mathrm{kl}}|}{|\tilde{V}_{ik}||\tilde{V}_{jl}|}. \tag{1.2.18}$$

The complex gains of the amplitudes cancel out, so, likewise with the phases, the true closure amplitude is identical. Each baseline samples two symmetrical points in the (u, v)-plane, leading to a discrete sampled observed visibility function $V_{\mathrm{obs}}(u, v)$ out of the complete continuous visibility function $V(u, v)$
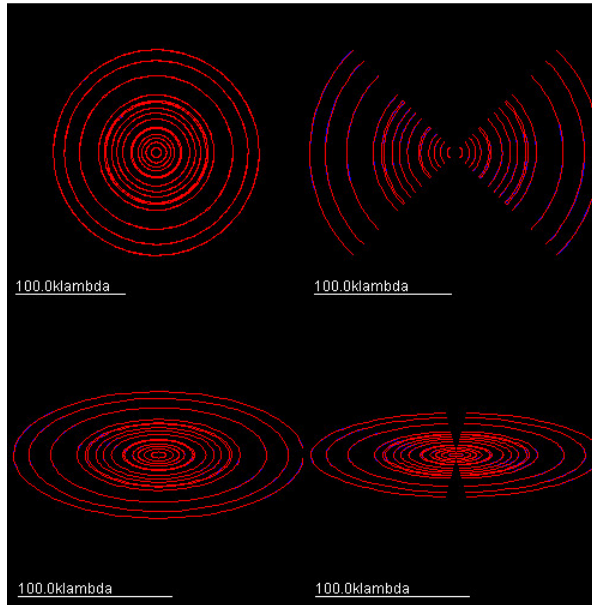
Figure 1.8.: Example (u,v)- planes showing the effects of observing time int the upper right panel, declination to the source in the lower left panel and a combined effect in the lower right panel. The image has been produced using the Virtual Radio Interferometer.

$$V(u,v) \times S(u,v) = V_{\mathrm{obs}}(u,v). \qquad (1.2.19)$$

$S(u,v)$ describes a spatial frequency transfer function and if convolution theorem gets applied, it means that our true brightness sky distribution carries the effect of a 'dirty beam' or point spread function. In order to maintain good image quality it is necessary to secure good sampling quality of the (u,v)-plane. Some typical artefacts stemming from the sampling quality are for example negative flux values or aliasing effects. In order to maintain a good sampling the arrays have to consist out enough telescopes. The number of baselines and hence data pairs in the (u,v)-plane scale quadratic with the amount of telescopes . In addition the rotation of the earth can be taken into account since the orientation of the telescope to the source changes with time and thus samples different points in (u,v)-space. This Earth rotation synthesis, or later shortened to aperture synthesis is also dependant on the declination to the target. For $\delta = 90°$ the measurements sample circles in the (u,v)plane which shapes into ellipses if the declination gets reduced. For declinations $\delta = 0°$ the sampling shapes into lines. Effects of the parameters are depicted in Fig. 1.8.

1.2.4. Mojave Data Sample and the VLBA

The MOJAVE program (Monitoring Of Jets in Active galactic nuclei with Vlbi Experiments) is dedicated to research radio jets in a sample of AGN. The most important
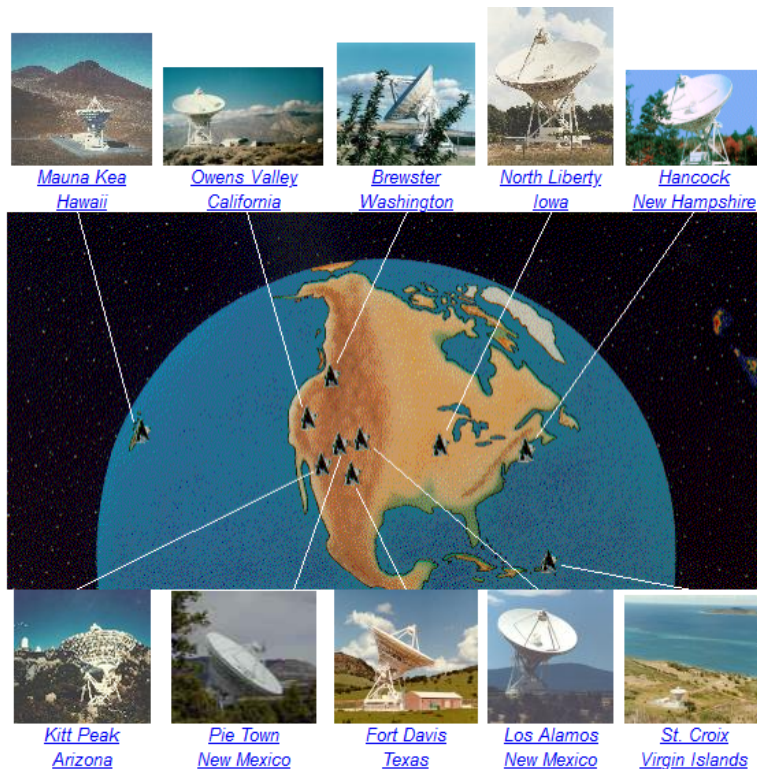
Figure 1.9.: The VLBA as an important array in the northern hemisphere with the 10 sites. Taken from the NRAO(http://www.vlba.nrao.edu/sites/)

science goals are to research the distribution of superluminal speeds and the intrinsic velocity, to resolve where the jet is collimated and accelerated and if the components follow the same trajectories as to mention a few of their vast research goals. In order for this to work they collect data of over 150 AGN with the Very Large Baseline Array (VLBA).

The VLBA consists of ten identical dishes with 25 m diameter each, located across the USA. Locations are in Brewster, Washington (B); Fort Davis, Texas (F); Hancock, New Hampshire (H); Kitt Peak, Arizona (K); Los Alamos, New Mexico (L); Mauna Kea, Hawaii (M); North Liberty, Iowa (N); Owens Valley, California (O); Pie Town, New Mexico (P) and St.Croix Virgin Islands (S). The telescopes span a baseline of 8611 km and observe in a frequency range of $0.3 - 96$ GHz. The array has an effective area of 19635 square kilometres and has therefore a sensitivity to measure brightness temperatures around 10^5 K. The VLBA provided the necessary radio data for this thesis.

1.3. X-ray Observations

The atmosphere of the earth is opaque in the X-ray regime, making it impossible to detect X-rays with ground based observations. In order to observe the X-ray sky, large telescopes has been sent to space. The following section covers the basics of X-ray observations and introduces the X-ray telescopes used in the analysis. It is based on the dissertation of Hirsch (2019) but further reference material will be highlighted.

1.3.1. Wolter Telescopes

The collection of X-ray photons, similar to optical ones, is achieved with mirrors. Snell's law describes the angle under which the photons leave the mirror

$$\frac{\sin \alpha_1}{\sin \alpha_2} = \frac{n_1}{n_2}. \tag{1.3.1}$$

α_1 describes the angle of the incoming photons, α_2 the outgoing angle. The refraction index n_1 can be neglected, since the photons travel through vacuum. For total reflexion to take place, α_2 has to be larger than $90°$ so the critical refraction angle is

$$\alpha_{\text{crit}} = \arcsin n_2 \tag{1.3.2}$$

The refraction depends on both the energy of the incoming photons and the material of the reflecting material, which scales with the size of the atoms. The energy in the X-ray regime is very high and even for the heavy materials like gold reflection angles are low. In order to increase the collection area Wolter (1952) introduced a set of mirrors which deflect the photons onto the same focus. To get a sharp image for on-axis and off-axis objects Abbe's sine condition has to be taken into account, where the distance from the mirror surface to the focus has to be equal for all paraxial rays. This can be achieved using two sets of mirrors consecutively like depicted in Fig.1.10.

The focused x-ray photons can then be detected by using charged coupled device (CCD). Further information can be found in Lesser (2015), but in principle a CCD is an array out of pixels, which each pixel consist out of an potential well. This is done by doping an silicon wafer with external atoms and thus creating a pn-junction. This creates a depletion zone where the electrons in the valence get away from the silicon leaving empty spaces. If a photon hits this pixel it frees the electrons in the depleted zone creating a current which can be read out.

### 1.3.2. X-Ray Telescope Programs

The X-ray observations analysed in this thesis were observed by two prominent X-ray telescope satellites. The Neil Gehrels *Swift* observatory (Gehrels et al., 2004) was launched on November 20, 2004. It consists out of several instruments but only XRT-data was used in this thesis. The XRT is a small Wolter telescope containing 12 nested
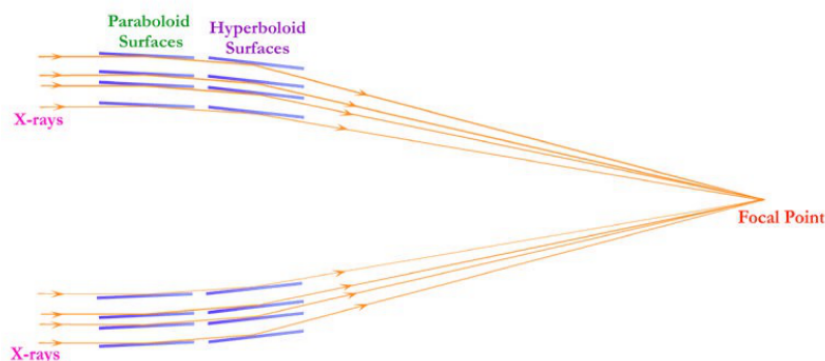
Figure 1.10.: Scheme of the principle of a Wolter telescope with four mirrors (http://chandra.harvard.edu/resources/illustrations/teleSchem.html

mirrors and operates in an energy band from $0.5 - 10\,\mathrm{keV}$. The camera uses European Photon Imaging Cameras (EPIC) MOS CCD at a focal length of 3.5m, similar to the MOS CCDs used on *XMM-Newton*. The Nuclear Spectroscopic Telescope Array (NuStar Harrison et al., 2013) launched in 2012 observes in an higher energy range of $3 - 79$ keV. It uses two multilayer coated Wolter 1 telescopes with a focal length of 10m. It uses one detectors included in each of the Focal Plane Modules A and B (FPMA,FPMB). Artist's impressions of both telescopes are shown in Fig.1.11a and Fig.1.11b.
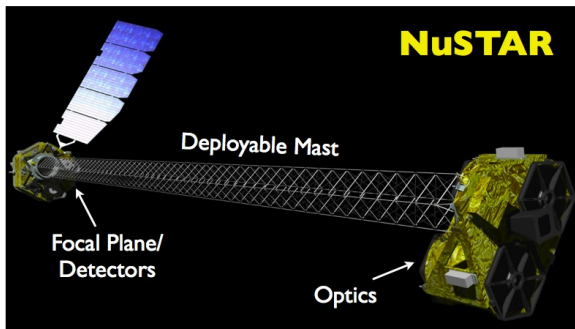
(a) Image of the NuSTAR telescope with highlights of certain components. https://heasarc.gsfc.nasa.gov/docs/nustar/
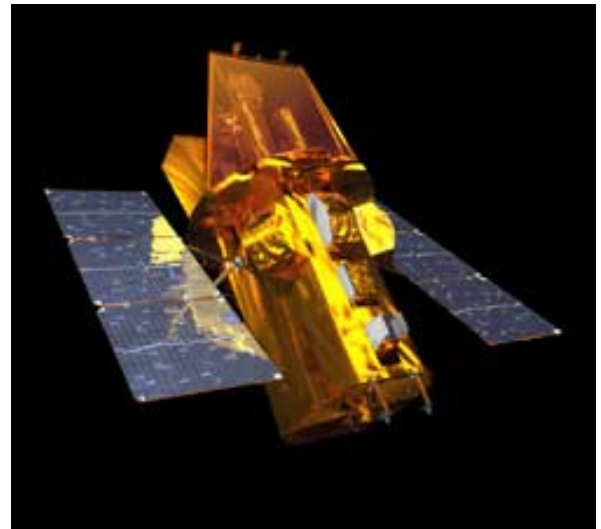
(b) Image of the Neil Gehrels *Swift* observatory. https://swift.gsfc.nasa.gov/

2. Radio Observations of 2043+749

To study the radio jet of 2043+749, data from the MOJAVE program were investigated. These data covers a time range from September 2016 to April 2019 in seven epochs and were observed at $15.3 Ghz$ by the VLBA.

2043+749 is placed at rectascension of 310.66 and a declination of 75.13 (**NED**) and is distanced around $z = 0.104$ away. An example of the (u, v)-coverage of the source is given in Fig.2.1. The remaining plots can be found in Appendix A. In most of the epochs the whole array was observing with the only two exceptions are the late epoch in 2017, where the Telescope Hancock is missing, and the observation in 2018, where St. Croix is missing. Although there some of the longer baselines are missed in those two epochs, the effects on the beam are not that significant and could be compensated. The baselines range around 800Mλ at a circular fashion, which leads likewise to an almost circular beam. The array parameters can be found in Tab.2.1.

2.1. Further Results

The MOJAVE group, which provided the data for this analysis, has also been working on a kinematic analysis of the radio data by the VLBA in parallel. This, however has not finally been published, so for reference Lister et al. (2018) will be given, while also a more detailed data archive can be found on their website [1]. They have found

---

[1] http://www.physics.purdue.edu/astro/MOJAVE/sourcepages/2043+749.shtml

Table 2.1.: Array configuration and resulting beam sizes for the observed period of 2043+749 with the VLBA at 15 Ghz. The telescopes have the corresponding abbreviations to Section 1.2.4.

Date	Array configuration	Beam size[mas]	Peak[Jy/beam]
26-09-2016	BFHKLMNOPS	0.650×0.606	0.168
06-11-2016	BFHKLMNOPS	0.654×0.617	0.178
10-12-2016	BFHKLMNOPS	0.854×0.747	0.168
28-01-2017	BFHKLMNOPS	0.702×0.603	0.162
25-08-2017	BFKLMNOPS	0.762×0.576	0.2
02-02-2018	BFHKLMNOP	0.719×0.664	0.222
15-04-2019	BFHKLMNOPS	0.672×0.608	0.203
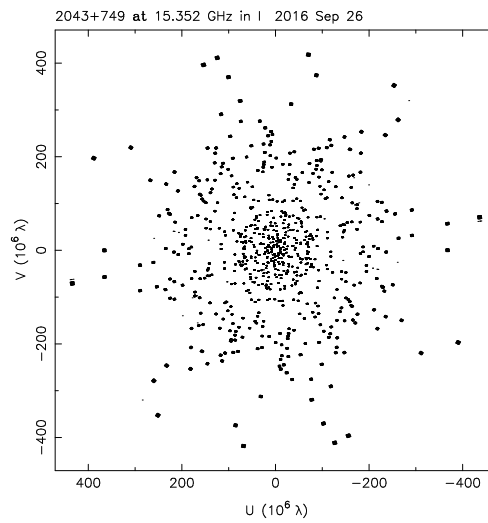
Figure 2.1.: Plot of the (u, v)-coverage of the first observation in September 2016.

a mildly subluminal outwards moving jet with an apparent speed of $v_{app} = (0.085 \pm 0.024)$mas/year or $\beta_{app} = (0.58 \pm 0.16)$. The separation or distance to the core plotted against the observation time can be found in Fig.2.2. They also modelled a spectral index map, which can be done by measuring the flux density at different frequencies and compare them to each other, the results for the spectral map are shown in Fig.2.3.
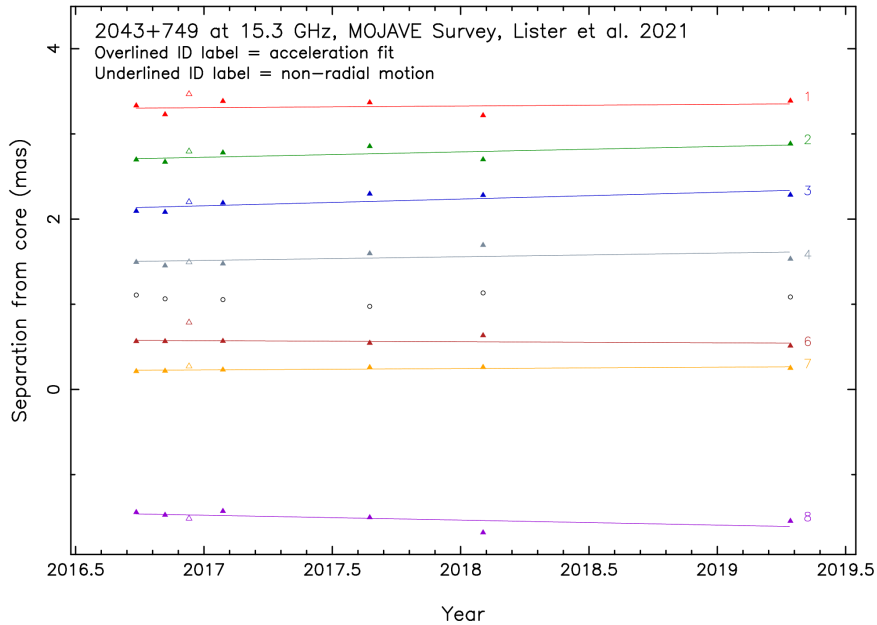
Figure 2.2.: Comparative jet kinematic scenario as proposed by the MOJAVE team.

2.2. Analysing VLBI-Data

To regain the intrinsic brightness distribution out of the observed visibility two steps are necessary: It has to be inversely Fourier transformed and deconvolved from the beam. Since the (u,v)-plane is not covered completely missing information has to be interpolated. An algorithm solving this constraints was introduced by Högbom (1974) which finds the solution in iterative fashion. The explanations for this CLEAN-algorithm follow after R. Cornwell T. B. and Briggs (1999).

1. The peak of highest intensity has to be found in the dirty image. This can be confined by setting CLEAN windows which restrict the peak to these.

2. At the peak position the intensity of the peak is multiplied with a dampening factor. This factor is called the loop gain and has to be smaller than $\gamma \leq 1$.
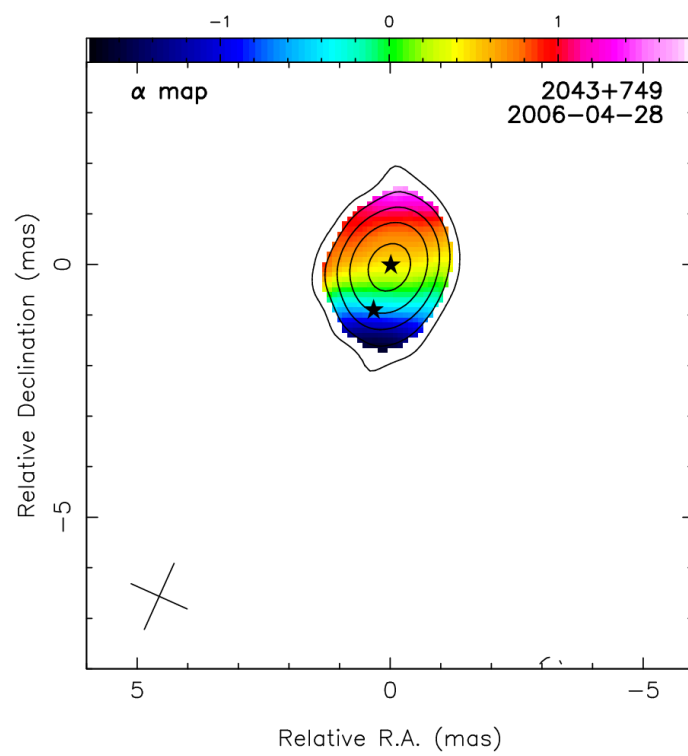
Figure 2.3.: Spectral index card of 2043+749, adapted from Lister et al. (2018).

3. The subtracted component has to be recorded in a δ-distribution with position and amplitude.

4. Repeat steps 1 to 3 until the dirty image is cleaned from intensities above the specified level and only the residuals remain.

5. Fit an elliptical Gaussian to the central lobe of the dirty beam to add as a CLEAN beam and convolve it with the found δ-distributions.

6. Add the remainder of the residuals in the CLEAN image.

In the process of the CLEAN-algorithm it can occur that some of the model components show negative intensity values, which would be non-physical. Therefore, the algorithm can be improved by adding physical constraints to the models. Also, the confinement of the structure would be neglected, which can be fixed through self-calibration based on the algorithm of Schwab (1980). This utilizes the over-determination of our interferometer to deal with residual phase and amplitude errors. The sum of squares of residuals is determined by the complex gains g_i and g_j

$$S = \sum_{i,j;i\neq j} w_{ij} |\tilde{V}_{ij} - g_i g_j^* \hat{V}_{ij}|^2, \tag{2.2.1}$$

where $\hat{V}_{ij}$ is the Fourier transformation of the sky intensity and w_{ij} resemble weighting factors reciprocal to the variance. This relation can be re-expressed to

$$S = \sum_{i,j;i\neq j} w_{ij} |\hat{V}_{ij}|^2 |X_{ij} - g_i g_j^*|^2, \tag{2.2.2}$$

with X_{ij} defined as

$$X_{ij} = \frac{\tilde{V}_{ij}}{\hat{V}_{ij}}. \tag{2.2.3}$$

By combining both algorithms our step-by-step solution gets expanded.

1. Follow the previous steps to produce a CLEAN-model but use constraints to the structure to keep it confined.

2. Find the transformation $\hat{V}_{ij}$ to convert our source into a point source.

3. Compute g_i and g_j and use them to calculate the corrected visibility.

4. Get the new CLEAN-image with the corrected visibility in accordance with the source structure.

5. Reiterate previous steps until a suitable model has been achieved.

The calibration of the amplitude and phase was done previously with the Astronomical Image Processing System (AIPS) provided by the NRAO and was not performed in this analysis. Nevertheless, more Information about this steps can be found in Zensus and Napier (1995). Further analysis has been done in DIFMAP (Shepherd, 2011), which implements both the CLEAN and the SELFCAL algorithm. DIFMAP provides several weighting options but only uniform weighting was used. This trades off sensitivity but keeps its focus on the longer baseline to maintain resolution. Thereafter the structure of a conical jet was modelled through rectangular CLEAN windows in order to confine the model to the physical structure and the first CLEAN-algorithm was performed. Then, the amplitudes and phases get self-calibrated over declining time-intervals with CLEANing steps in between. The last step was to deep-CLEAN the remaining flux and an image was produced. This has been performed on every single epoch of the analysed data.
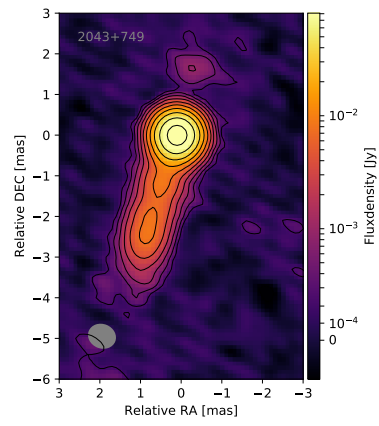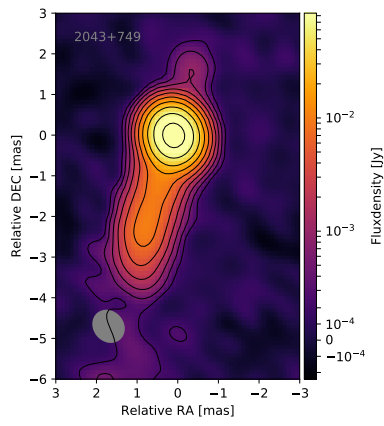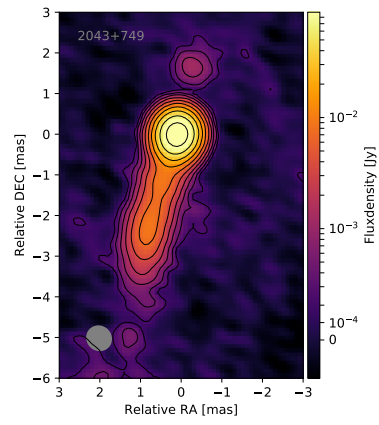
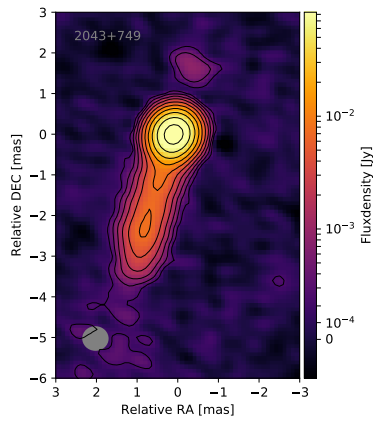## 2.3. Imaging and Modelfitting

The imaging process were conducted as described in Section 2.2 with CLEAN ans SELFCAL-algorithms and resulted in Fig. 2.4. These are consistent with the images produced by the MOJAVE collaboration of Lister et.al which have not been officially published until now. The source features a bright core, which showed almost no change in flux over the course of the observations. Connected to the core, there is a bright continuous jet moving towards the observer . Also visible is a fainter counter-jet in the opposite direction which shows only one component in most of the epochs and is not continuous. Further downstream of the jet, some diffuse emission is found, which shows no characteristic feature and could not be tracked due to the low significance compared to the noise level.

With the produced radio cards, the next step is to track the components or 'blobs' in the images. This can be done by fitting two dimensional Gaussian components at first to the core region and then iteratively to the remaining visibilities, in a similar fashion to the δ-components. These components are more stable for the brighter ones. Therefore, it is possible to fit the core with an elliptical component, the jet features however could only be fitted with circular components. In the jet five features could be found, which could be tracked over all epochs. The fainter counter jet can only be fitted with one component. A further elliptical component is fitted further downstream to simulate the faint diffuse emission. However, this component will not be used for tracking purposes. The results of the model fitting can be found in Fig.2.5 and in Tab. A.1.

The model-fit-algorithm used in this analysis uses the method of maximum likelihood, which is, according to Fomalont (1999), given by the variance σ^2 if all errors are distributed equally
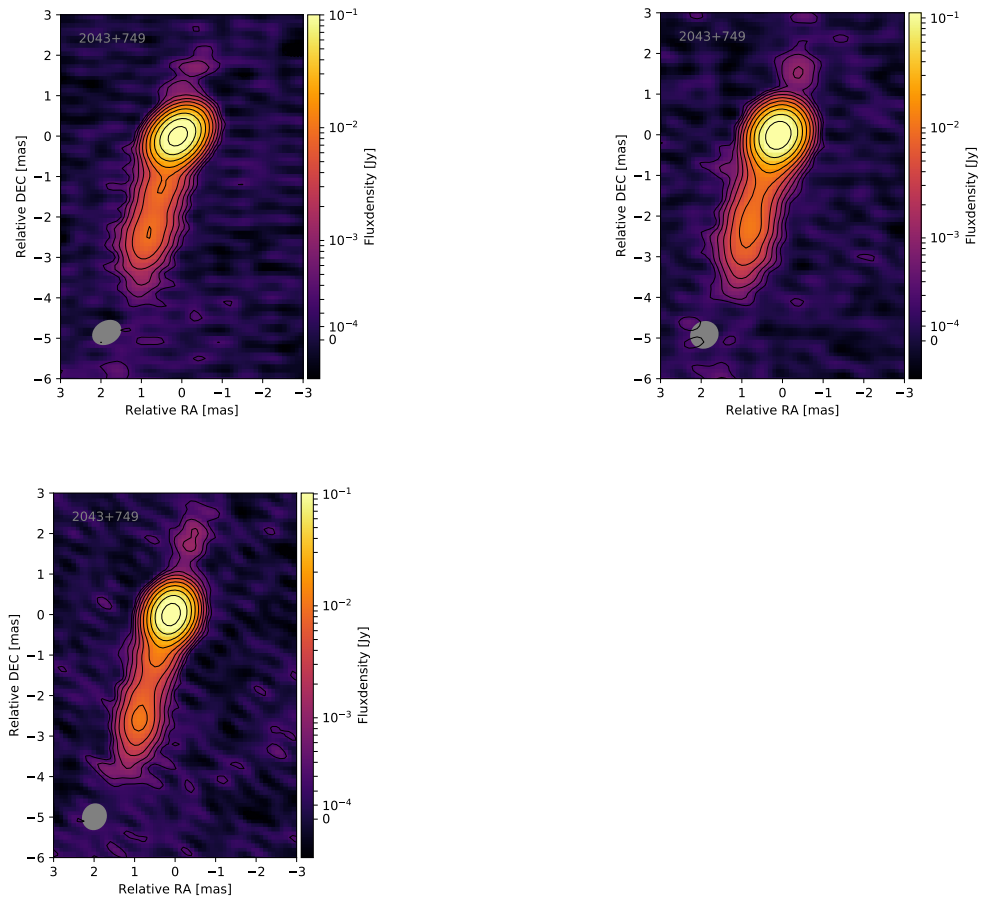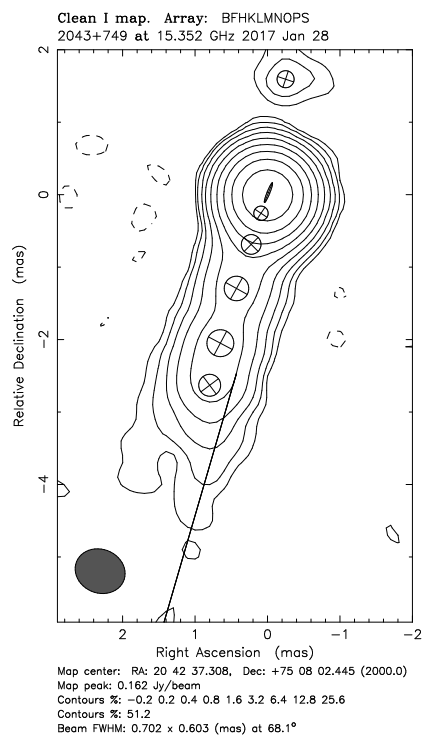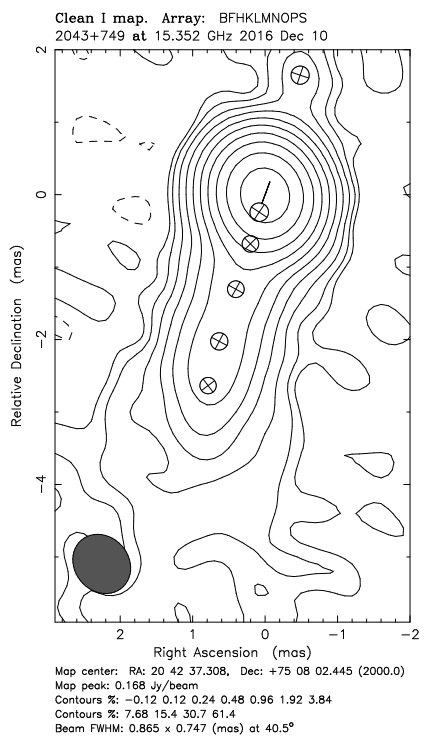
$$\sigma^2 = \sum (M(p_j; i) - I(l_i))^2. \tag{2.3.1}$$

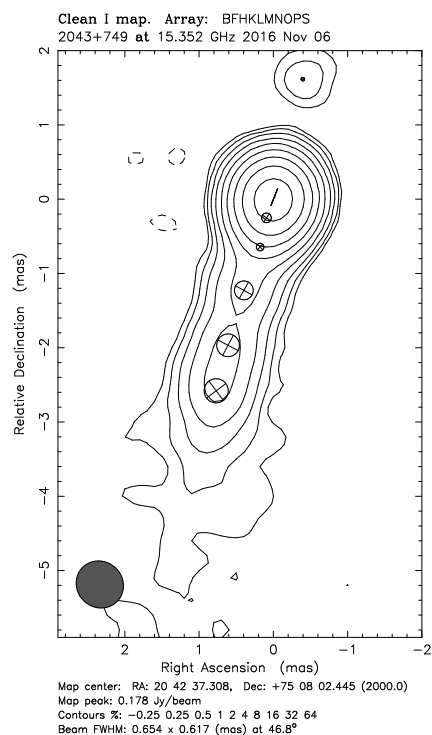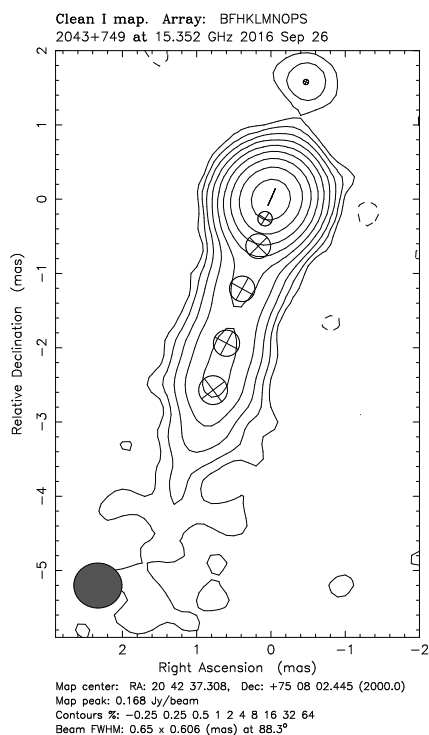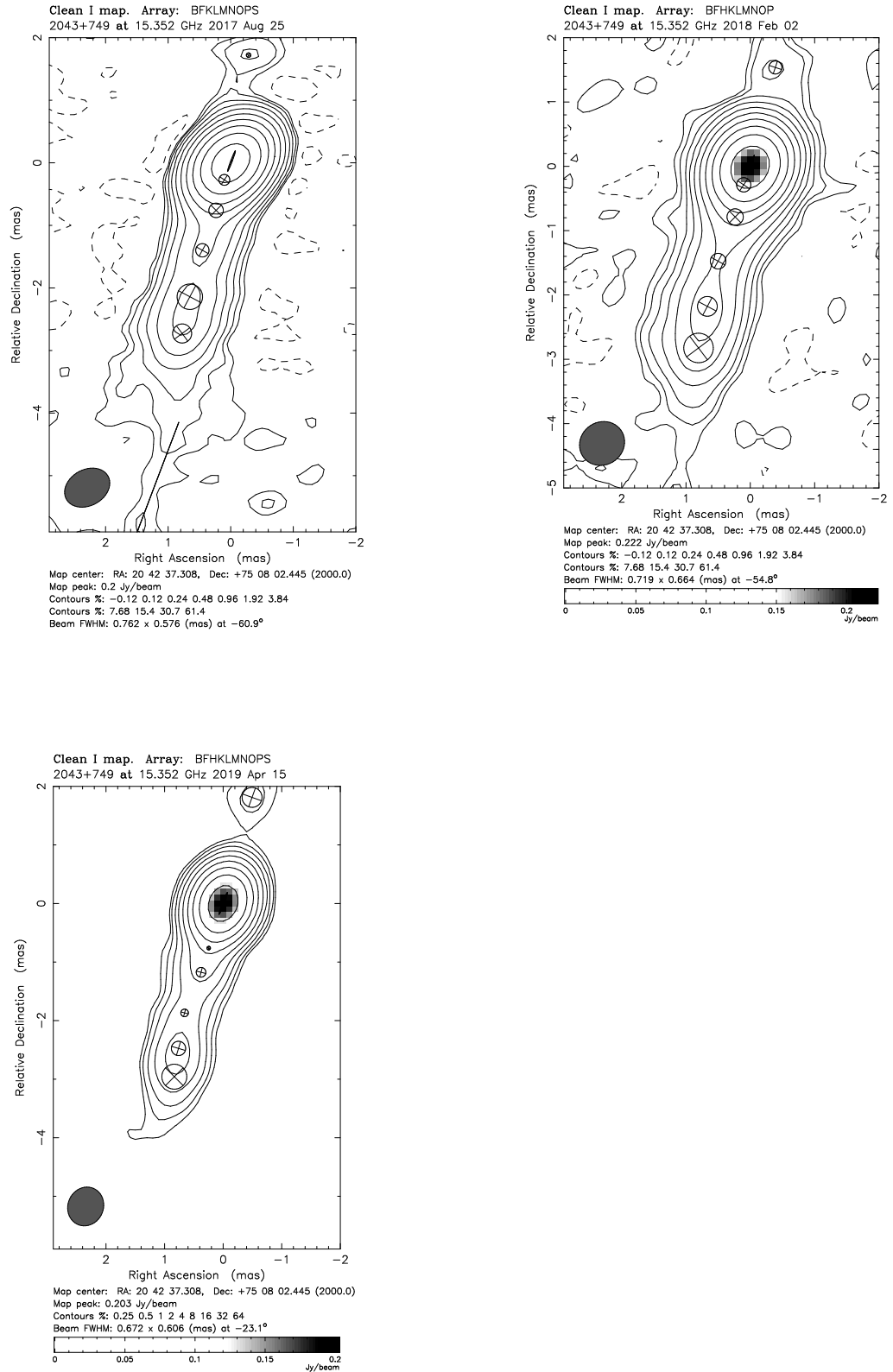34

Figure 2.4.: Clean Images of 2043+749 for the seven epochs of the main analysis in the period from 2016 to 2019 ordered in chronological fashion.

Clean I map. Array: BFHKLMNOPS
2043+749 at 15.352 GHz 2016 Sep 26

Relative Declination (mas)
Right Ascension (mas)
Map center: RA: 20 42 37.308, Dec: +75 08 02.445 (2000.0)
Map peak: 0.168 Jy/beam
Contours %: −0.25 0.25 0.5 1 2 4 8 16 32 64
Beam FWHM: 0.65 x 0.606 (mas) at 88.3°

Clean I map. Array: BFHKLMNOPS
2043+749 at 15.352 GHz 2016 Nov 06

Relative Declination (mas)
Right Ascension (mas)
Map center: RA: 20 42 37.308, Dec: +75 08 02.445 (2000.0)
Map peak: 0.178 Jy/beam
Contours %: −0.25 0.25 0.5 1 2 4 8 16 32 64
Beam FWHM: 0.654 x 0.617 (mas) at 46.8°

Clean I map. Array: BFHKLMNOPS
2043+749 at 15.352 GHz 2016 Dec 10

Relative Declination (mas)
Right Ascension (mas)
Map center: RA: 20 42 37.308, Dec: +75 08 02.445 (2000.0)
Map peak: 0.168 Jy/beam
Contours %: −0.12 0.12 0.24 0.48 0.96 1.92 3.84
Contours %: 7.68 15.4 30.7 61.4
Beam FWHM: 0.865 x 0.747 (mas) at 40.5°

Clean I map. Array: BFHKLMNOPS
2043+749 at 15.352 GHz 2017 Jan 28

Relative Declination (mas)
Right Ascension (mas)
Map center: RA: 20 42 37.308, Dec: +75 08 02.445 (2000.0)
Map peak: 0.162 Jy/beam
Contours %: −0.2 0.2 0.4 0.8 1.6 3.2 6.4 12.8 25.6
Contours %: 51.2
Beam FWHM: 0.702 x 0.603 (mas) at 68.1°

37

Clean I map. Array: BFKLMNOPS
2043+749 at 15.352 GHz 2017 Aug 25

Map center: RA: 20 42 37.308, Dec: +75 08 02.445 (2000.0)
Map peak: 0.2 Jy/beam
Contours %: −0.12 0.12 0.24 0.48 0.96 1.92 3.84
Contours %: 7.68 15.4 30.7 61.4
Beam FWHM: 0.762 x 0.576 (mas) at −60.9°

Clean I map. Array: BFHKLMNOP
2043+749 at 15.352 GHz 2018 Feb 02

Map center: RA: 20 42 37.308, Dec: +75 08 02.445 (2000.0)
Map peak: 0.222 Jy/beam
Contours %: −0.12 0.12 0.24 0.48 0.96 1.92 3.84
Contours %: 7.68 15.4 30.7 61.4
Beam FWHM: 0.719 x 0.664 (mas) at −54.8°

Clean I map. Array: BFHKLMNOPS
2043+749 at 15.352 GHz 2019 Apr 15

Map center: RA: 20 42 37.308, Dec: +75 08 02.445 (2000.0)
Map peak: 0.203 Jy/beam
Contours %: 0.25 0.5 1 2 4 8 16 32 64
Beam FWHM: 0.672 x 0.606 (mas) at −23.1°

Figure 2.5.: Radio images of 2043+749 with fitted two dimensional components to track the movement in the radio jet.

This means that the major axis of a component can diverge in theory, however in reality we are confined by the resolution of the array. According to Kovalev et al. (2005), the resolution limit can be calculated by

$$\Theta_{\text{lim}} = b_\psi \sqrt{\frac{4 \ln 2}{\pi} \ln \left(\frac{SNR}{SNR - 1} \right)}, \qquad (2.3.2)$$

where b_ψ is defined by the size of the beam in direction to the axis. The SNR is the signal-to-noise ratio and can be measured by calculating the flux density in the vicinity of the source and is comparing it to the flux density of the components. Components are resolved if the axis of the component is larger than the resolution limit. The resolved components can be compared to the radiation of a black-body by computing the brightness temperature of the component which is, according to Kovalev et al. (2005), given by

$$T_b = \frac{2 \ln 2}{\pi k} \frac{S_{\text{Core/Component}} \lambda^2 (1 + z)}{\Theta_{\text{maj}} \Theta_{\text{min}}}. \qquad (2.3.3)$$

Θ_{maj} and Θ_{min} are the minor and major axis of the model-fit components. The positions and parameters for all fitted components can be found in Tab. A.1.

2.4. Kinematic Analysis

To investigate the movement of the components, the position relative to the core component is calculated. This is done by converting the given polar-coordinates to Cartesian coordinates and subtract the position of the core component. Based on the assumption on a conical jet, in which jet components are accelerated shortly after the ejection into the jet and move at an constant velocity afterwards, the model components can be fitted by a linear model. The only difficult task is to identify the right component, which is often non-distinctive. The fitted model offers two possible solutions how the components can be identified. Therefore, two different scenarios will be described in the following.

First Scenario

In the first scenario the components are identified by their distance to the core component, except for the counter-jet component which was identified by the direction to the core component. This leads to mildly superluminal motion outwards. Based on this scenario the distances are plotted against the time-axis in Fig. 2.6. The resulting speeds are shown in Tab. 2.2.

The speed of the components is pretty close to a linear function,which is also shown by the reduced χ^2 values. Most of the components have a χ^2 value of lower than one
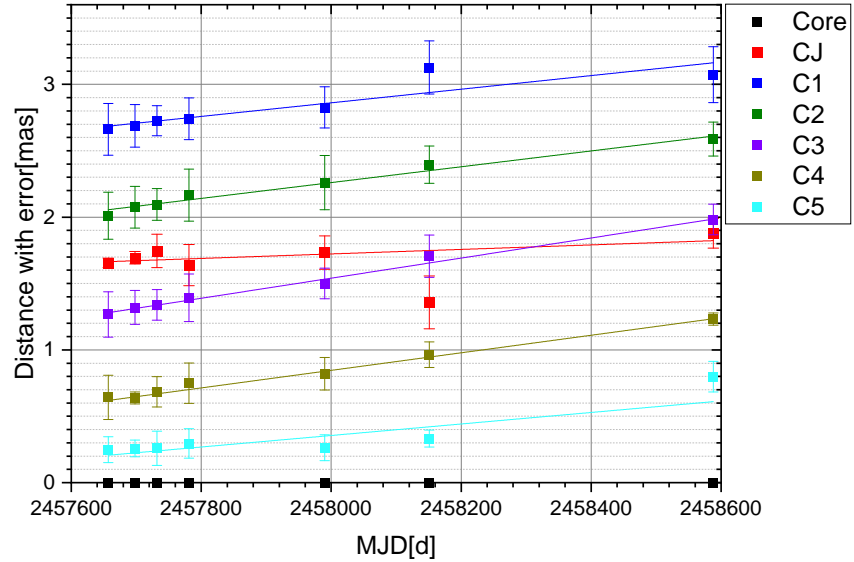
Figure 2.6.: Distance of the components relative to the core component dependant on the observation time. The uncertainty is based on the major axis of the component which resembles the FWHM of the component.

Table 2.2.: Results for the apparent speed, the apparent speed in relation to the speed of light and the reduced χ^2 for the first scenario.

Component	$v_{\mathrm{obs}}[\mathrm{mas}]$	$\Delta v_{\mathrm{obs}}[\mathrm{mas}]$	β_{app}	$\Delta\beta_{\mathrm{app}}$	χ^2_{red}
CJ	0,062	0,042	0,423	0,287	0,962
C1	0,187	0,041	1,277	0,277	0,227
C2	0,217	0,013	1,484	0,091	0,048
C3	0,276	0,011	1,886	0,076	0,041
C4	0,241	0,005	1,646	0,037	0,047
C5	0,158	0,048	1,080	0,326	1,217
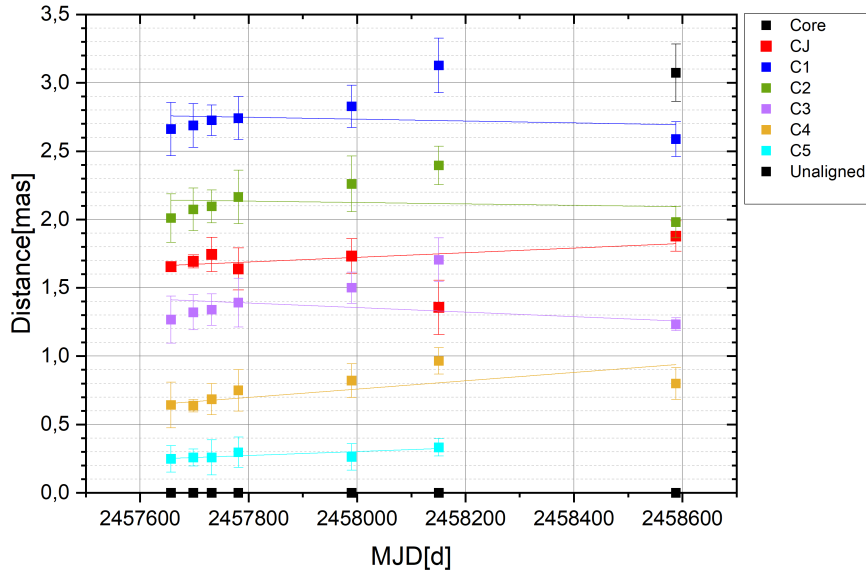
Figure 2.7.: Distance of the components relative to the core component dependant on the observation time. The identification of the components has changed in the last epoch, which leads to a slower behaviour. The error is based on the major axis of the component which resembles the FWHM of the component.

which statistically implyies that the uncertainties are overestimated. The uncertainties are based on the size off the major axis, the FWHM of the jet-component.

Second Scenario

The second scenario compares the model to the subluminal speeds found by Lister et al. (2018) and rearranges the components in the last epoch. This leaves most of the components with negative speeds, which would imply, that they are moving backwards to the core. Due to the high deviation of the linear fit, the uncertainty is not excluding stationary components, which would be possible as shown by Jorstad et al. (2017). The only component, which is also the fastest component,that matches the proposed velocities of Lister et al. (2018) is C4 and will be discussed later.

2.5. Brightness Temperature and Flux Density

As shown in Fig. 2.8, the core component shows a slight increase in flux density. The relative uncertainty of the flux density is estimated to be 5% for the VLBA. The components showed no variation in flux density over the observed time frame except for C5,

Table 2.3.: Observed speed, apparent speed relative to the speed of light and the reduced χ^2 values for the second scenario.

Component	$v_{\mathrm{obs}}[\mathrm{mas}]$	$\Delta v_{\mathrm{obs}}[\mathrm{mas}]$	β_{app}	$\Delta\beta_{\mathrm{app}}$	χ^2_{red}
CJ	0,0620	0,042	0,423	0,287	0,962
C1	-0,025	0,065	-0,171	0,442	1,12
C2	-0,019	0,064	-0,128	0,435	1,23
C3	-0,061	0,045	-0,414	0,308	1,76
C4	0,111	0,045	0,759	0,308	1,00
C5	0,053	0,015	0,361	0,099	0,056

which has a slight dip in the last epoch. The jet-component near the core is brighter but the further components show a pretty steady level of flux density. The counter-jet component shows the weakest flux density.

The brightness temperature of the core component varies around the inverse Compton limit of $T_b \sim 1^{12}\,\mathrm{K}$, which is shown in Fig. 2.9. Some jet-components show a very high brightness temperature. The calculation of the resolution limit shows that the major axes of these components are below the resolution limit or pretty close-by. Therefore, they can be neglected for the brightness temperature. Only three values for the brightness temperature of the core component could be calculated, the rest had a diverging axial ratio. The Results for the brightness temperature of the different jet, counter-jet and core components are shown in Fig. 2.10 for the distance to the core component. Note that the component identification of the first scenario is used for the plots of the brightness temperature and flux densities.
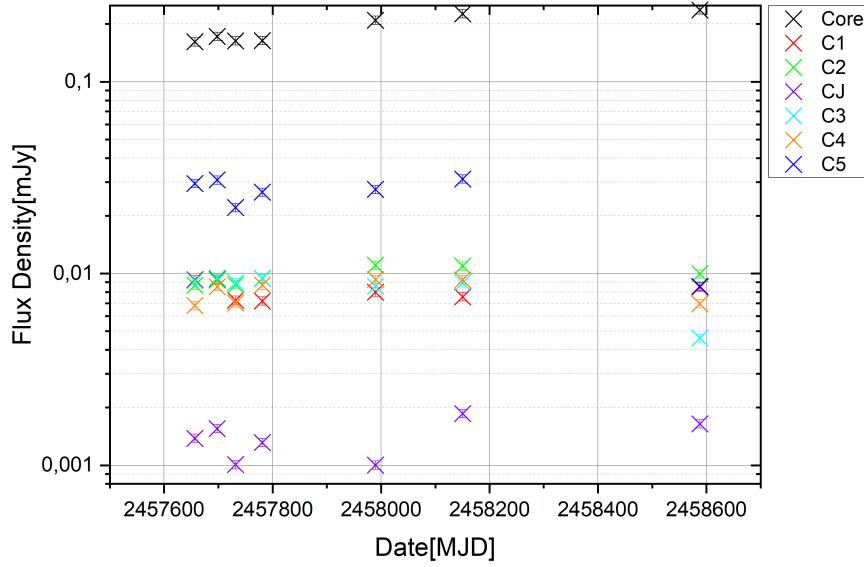
2.6. Inclination Angle

With Eq.1.1.28 and Eq.1.1.31 a connection between the jet-to-counterjet ratio and the apparent speed can be drawn to

$$\Phi = \arctan\left(\frac{2\beta_{\mathrm{app}}}{R^{1/p}-1}\right). \tag{2.6.1}$$

It was always used the fastest component for the calculation of the inclination in all three scenarios. This was C3 in the first scenario with an $\beta_{\mathrm{app1}} = 1.886$ and C4 in the second scenario with $\beta_{\mathrm{app2}} = 0.76$, which also came closest ot the speed of Lister et al. (2018). For the Lister-scenario the fastest component was given by $\beta_{\mathrm{app3}} = 0.58$. The results for the inclination angles are shown in Tab.2.4 with the flux density evaluated by calculating the mean of the jet over all epochs and the spectral index $\alpha = 0.5$ taken out of the spectral card in Fig.2.3 as part of the results of Lister et al. (2018). Since the flux density was taken for the whole jet it is independent on the model and therefore,
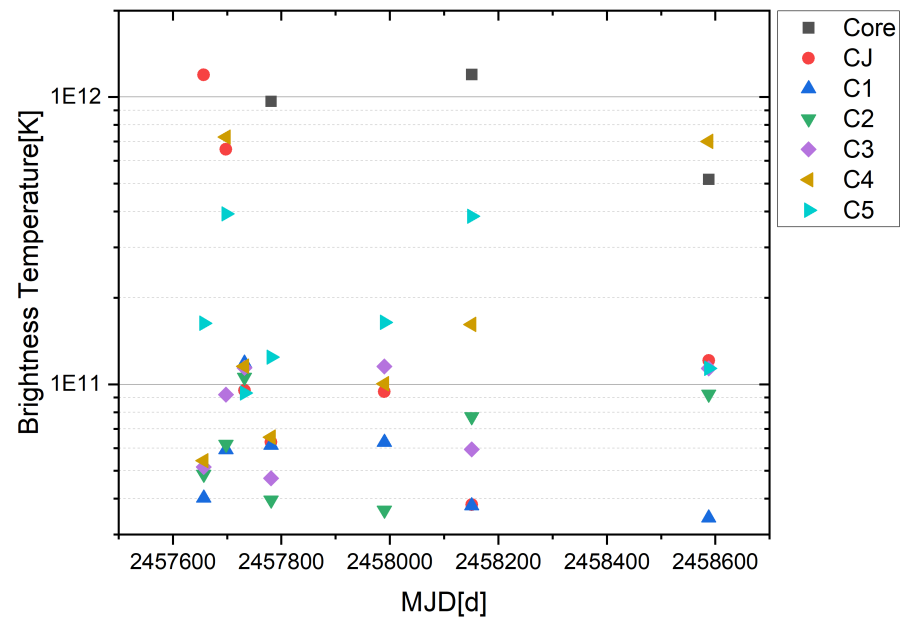
Figure 2.8.: Flux density of all model components over all epochs, for better comparison on a logarithmic scale.
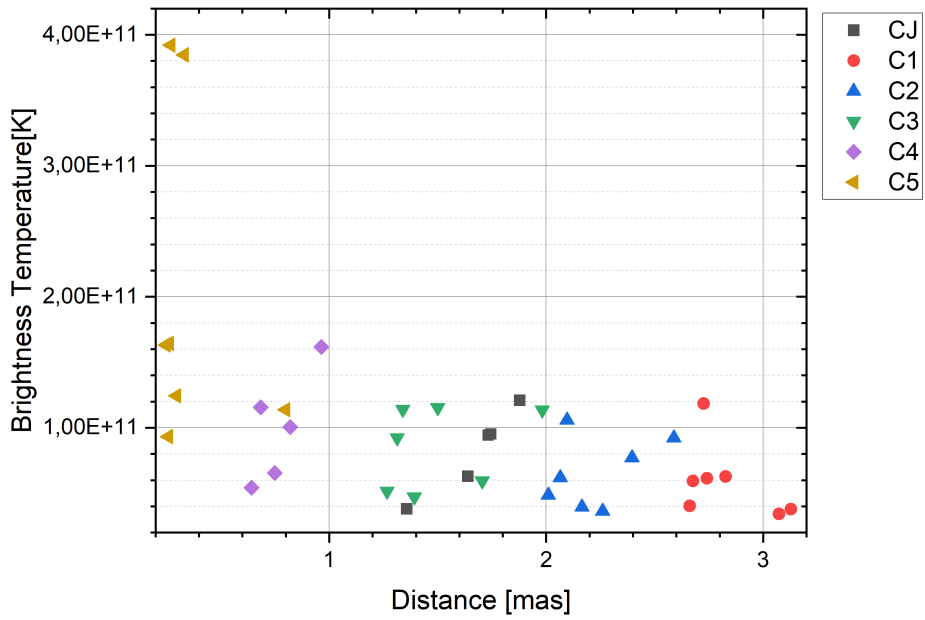
for all scenarios the same.

Table 2.4.: Table showing the derived inclination angles from the three presented models.

Model	β_{app}	S[mJ/beam]	Φ[deg]
First	1.89	9.56	47
Second	0.76	9.56	23
Lister	0.58	9.56	18

Figure 2.9.: Brightness Temperature of all model components over the different epochs plotted against an logarithmic scale.

Figure 2.10.: Brightness temperature of the components in relation to the distance to the core component.

3. X-ray Observations of 2043+749

In this Section the focus shifts from radio to X-Ray observations. As stated earlier there are no ground based X-ray telescopes and observations have to be done from space. For the X-ray observations, used for the spectral analysis of this thesis, four observations of *NuSTAR* have been taken in combination with one *Swift*/XRT observation. While *NuSTAR* covers the hard X-ray from $3.0 \, \text{keV}$ to $80 \, \text{keV}$, *Swift*/XRT has more sensitivity in the soft X-ray bands and covers energies from $0.5 \, \text{keV}$ to $10.0 \, \text{keV}$. This is defined by the effective area of the corresponding X-ray telescope. More information about the observed data can be found in Tab.3.1.

3.1. Data Extraction

The first step is to calibrate and extract the data of the observations. For NuSTAR this can be achieved by using the nupipeline, which is part of the heasoft package provided by the nasa. For calibration of the data the NuSTAR FPM caldb 20201130 was used. After the calibration, a source and a background region have to be defined. The source region has to include all photons of the source and was placed around the central peak of radiation with an radius of 50 arcsec. The background region was placed in the vicinity of the source to get the most accurate result for the background photons, with a radius of 70 arcsec. ISIS uses the background photons to modulate the influence of the background into the spectrum. Similar steps were conducted for the *Swift*/XRT data, which is also part of the heasoft package. The calibration database Swift XRT caldb was on version 20200704. In Fig. 3.1, the detector image of FPMA shows the source compared to the circular sourceregion and the upper left background extraction region.

Table 3.1.: X-Ray observations analysed in this thesis. Four *NuSTAR* observations were used with the given exposure times and one XRT observations, which started parallel to the first *NuSTAR* observation.

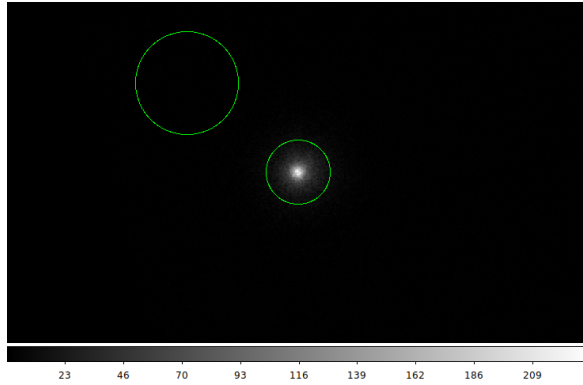| Instrument	ObsID	Exposure Time[ks]	Start Date
NuSTAR	60001080002	17	21-09-2014
NuSTAR	60001080004	53	22-09-2014
NuSTAR	60001080006	82	30-10-2014
NuSTAR	60001080008	39	22-12-2014
Swift/XRT	00080795001	2	21-09-2014

Figure 3.1.: X-ray image of 4c 74.26.

3.2. X-Ray Models

In this Section the three main models used for the analysis will be discussed based on their different parameters. The first model, the *pexmon* model, describes a reflected powerlaw in a neutral medium and combines it with some of the most important emission lines. The second model, the *relxill* model, is also capable of modelling reflection but enhances it with relativistic effects and it adds a lamppost geometry, which will be useful for studying the jet-accretion disc interaction. The last model *tbnew*, describes the galactic absorption in our host galaxy caused by abundances of hydrogen and other elements.

3.2.1. Pexmon

The *pexmon* model (Nandra et al., 2007) is based on reflection in a slab geometry. Here the parameters of the model will be given in a short list:

1. Photon index γ
2. Cut-off energy E_c
3. Reflection scaling factor
4. redshift z
5. Abundance of heavier elements A
6. Abundance of iron A_{Fe}
7. Inclination angle i
8. Norm

The continuum is modelled by a power law γ, which is cut exponentially above an energy treshold E_c. Through the abundance of iron a reflection component is added at

an energy of 6.4 keV, which depends on the photon index, the inclination to the observer, and the abundance of the iron itself, which is given relative to solar units. It is useful to define an equivalent width, which uses the height of the spectral line and compares the area deviating to the continuum with an rectangle. The parametrization is then given by

$$EW = 9.66 EW_0(\gamma^{-2.8} - 0.56), \quad 1.1 < \gamma < 2.5. \tag{3.2.1}$$

The inclination dependence can be approximated by a cubic fit

$$EW = EW_0(2.20 \cos i - 1.749 \cos^2 i + 0.541(cos^3 i)i < 85 \deg \tag{3.2.2}$$

The abundance itself is parametrized logarithmic by

$$\log EW = \log EW_0[0.641 \log A_{\mathrm{Fe}} - 0.172(\log A_{\mathrm{Fe}}], \quad 0.1 < A_{\mathrm{Fe}} < 10. \tag{3.2.3}$$

3.2.2. Relxill

The *relxill* model (Garcia et al., 2014) combines the reflection spectrum of an ionized accretion disk and an angular dependent reflection of X-ray emission.

The parameters used in the parametrizationare given in this short list:

1. Black-hole spin a

2. Ionization of the accretion disk $\log \xi$

3. Inner and outer radius of the accretion disk in units of ISCO R_{in}, R_{out}

4. Inclination i

5. Iron abundance A_{Fe}

6. Cut-off energy E_{c}

7. Photon index γ

8. Redshift z

9. Height of primary source above accretion disk h

10. Norm

Similar to the *pexmon* model, the basic geometry is described by a slab geometry of the accretion disk. Light falls onto the accretion disk by a lightsource, i.e. the jet, and gets reflected in the atmosphere of the accretion disk. The amount of reflected photons received from the observer however is dependent on the inclination angle of the source. In addition, the material in the accretion disk is highly relativistic and ionized, which also takes effect on the reflected spectra.

3.2.3. Tbnew

The last model,*tbnew* [1] is based on *tbabs* (Wilms, Allen, and McCray, 2000), implements glactic absorption of all abundances in the evaluation by taking into consideration that our host galaxy has large amounts of hydrogen and some other elements, which absorb some of the X-ray emission in the interstellar Medium (ISM). The cross section of all absorbing mass can be described by

$$\sigma_{\mathrm{ISM}} = \sigma_{\mathrm{gas}} + \sigma_{\mathrm{molecular}} + \sigma_{\mathrm{grains}}. \tag{3.2.4}$$

All impact of all elements is normed to the density of hydrogen N_{H} and therefore the intensity of the source relates to the observed intensity

$$I_{\mathrm{obs}} = \exp(\sigma_{\mathrm{ISM}}(E)N_{\mathrm{H}})I_{\mathrm{source}}. \tag{3.2.5}$$

The most important absorber by far is hydrogen and therefore the variation of the model *Tbnew_simple* was used, which only has an input- or fit-parameter for the hydrogen density column, while it uses the values given in Wilms, Allen, and McCray (2000) for the other abundances.

3.3. Reproduction of Previous Results

To first step of the analysis of X-ray models in this thesis, is followed after the steps taken by Lohfink et al. (2017), which also made some efforts to understand the spectrum of the observed source. This was done in order to derive a baseline model, which could be used in modelling the X-ray spectrum of 2043+749 with the results gained out of the radio analysis.
For this the *NuSTAR* data of the four observations was stacked together for each detector, loaded in `ISIS`and rebinned to a count rate of 100 per bin, which translates to a signal-to-noise ratio of 10. This was combined with the data of *Swift*/XRT with the same binning leading to three datasets. The model Lohfink et al. (2017) used is based on the models described in the previous Section 3.2 and combines them with following equation

$$(relxilllp \cdot pexmon \cdot tbnew\_simple). \tag{3.3.1}$$

The different datasets are coupled with a constant factor to correct for the cross-correlation in-between and free norm values. Since both the *Relxill* and the *Pexmon* model are capable to model the reflection continuum, which might interfere with each other, the reflection parameter was switched off in the *Relxill* model. To further improve the simulation of jet-physics an variant of the *Relxill* model was used, which is specialized in modelling a lamppost geometry (*rellxilllp*). The results for the best-fit parameters

---

[1] https://pulsar.sternwarte.uni-erlangen.de/wilms/research/tbabs/

of Lohfink et al. (2017) and my reevaluation are shown in Tab. 3.2, and the photon counts with their residuas are shown in Fig.3.2. Note that only one XRT-observation is included in the data of the thesis in comparison to the XRT-data in Lohfink et al. (2017) where more observations were included. The results are pretty similar, but do not match exactly. Since some of the parameters by Lohfink et al. (2017) were only given in intervals it was not possible for those parameters to match the exact input they used, which could explain the small difference to the re-evaluation. Also, the innermost stable radius of the accretion disk was fixed to the minimal value since it interferes with the fit of the black-hole spin, because they are highly correlative to each other.

Table 3.2.: Comparison of parameters between the best-fit model of Lohfink et al. (2017), the Parameters marked with x were fixed to that value.

	Parameter	Lohfink	Result
Absorption	N_H	<2.3	3.1
Continuum and	γ	1.81	1.81
Cold reflection	E_{cut} [keV]	183	190
Ionized Reflection	h [ISCO]	7	26.7983
	Rin [ISCO]	14	1 x
	a	uncont.	0.-998
	i	35	35 x
	A_{fe}	1.0	0.56
	$\log \xi$	2.7	2.8
Norm	$N - rel$	3.6	1.8
	$N - pex$	<2.0	3.7
Red. χ^2		1.0783	1.08917

3.4. Adapting a new Inclination angle

The model found in the previous section was now combined with the inclination angles of the radio observations found in Section 2.6. The inclination of both kinematic models and the inclination angle derived from the studies of Lister et al. (2018) were included in the model-calculation. The starting parameters for the simulation were taken from the output of the Lohfink et al. (2017) model. The results of all inclination simulations stayed in good agreement to each other and showed no big deviations. The output parameter are shown in Tab. 3.3 in the residuals between the photon count and the model are shown in Fig. 3.3. To estimate errors of the parameters the confidence intervals of the parameters were calculated for the 2σ confidence interval of the shown parameters.
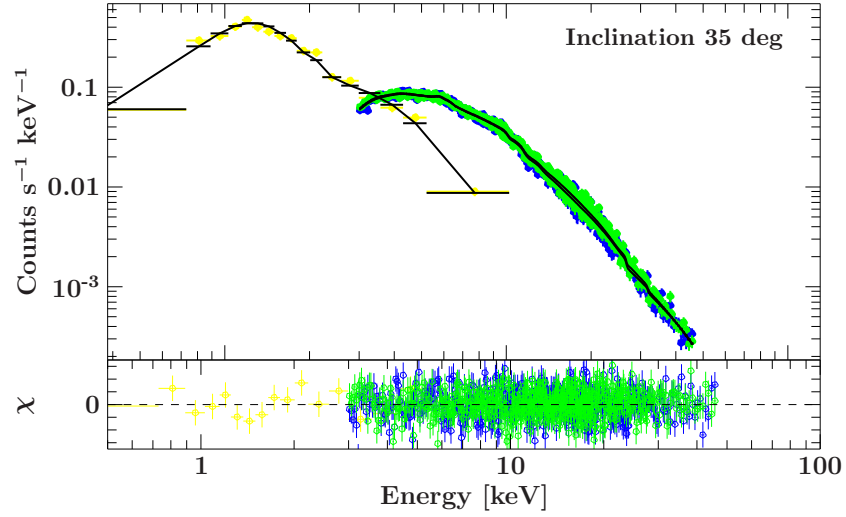
Figure 3.2.: X-ray spectrum with the reproduced model. The absolute residuals are plotted in the bottom. The black lines at the XRT-data indicate the bin-range for the energy.
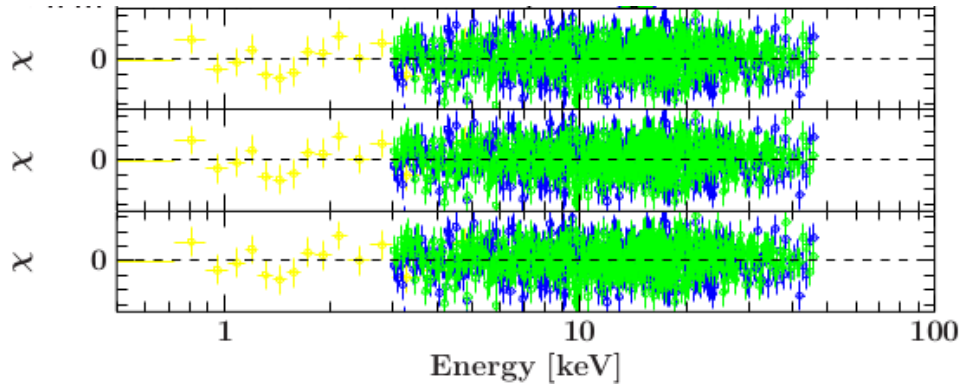
Figure 3.3.: Residuals of the Model-fit for the inclinations of 18°,23° and 47°.

Table 3.3.: Fitparameters for the three different Inclinations showing the free parameters, their value and the 2σ confidence intervals.

Inclination	18 deg			23 deg		
Parameter	best	min	max	best	min	max
h	16.9402	3	61.9658	15.9448	3	65.7441
a	-0.998	-0.998	0.998	-0.998	-0.998	0.998
γ	1.81244	1.78931	1.85074	1.8163	1.77642	1.85497
$\log\xi$	2.84683	2.12024	3.54571	2.82636	2.00943	3.06852
A_{Fe}	0.602647	0.5	0.884813	0.605911	0.5	0.945181
E_{cut}	149.688	195.837	280707	195.729	150.773	278.58
χ^2	1130.479444			1130.217742		
red. χ^2	1.088046			1.087794		

Inclination	35 deg			47 deg		
Parameter	best	min	max	best	min	max
h	26.7968	3	100	3.83473	3	100
a	-0.998	-0.998	0.998	-0.599006	-0.998	0.998
γ	1.81419	1.80826	1.86175	1.81245	1.77197	1.85591
$\log\xi$	2.80188	0	3.18835	3.08224	1.85172	3.23846
A_{Fe}	0.564673	0.5	0.8914	0.54561	0.5	0.787789
E_{cut}	190.134	120.776	273.135	190.776	136.99	276.748
χ^2	1131.649549			1130.165572		
red. χ^2	1.089172			1.087744		

4. Discussion

So far, the radio observations have described three different plausible scenarios for the kinematic of the jet. Therefore, it is necessary to weigh the options and to take the X-ray observations into account.

4.1. Conclusion of the X-ray analysis

The analysis of the X-ray observations utilized the three different inclination angle scenarios of the radio analysis. All three scenarios were significantly consistent with the re-evaluation of Lohfink et al. (2017) and proofed capable to be reasonable inclination angle results. This was shown via the reduced χ^2 values, which were all close to 1 and were only distinguishable after the fourth digit. The parameters, apart from the inclination angle, showed an overlap in their confidence intervals, which also proofs to be reasonable.

To further test the X-ray model an analysis over the whole parameter space was conducted. In an ideal case, the χ^2 landscape would be fairly simple and the best-fit value is found in the global minimum. When stepping through the whole range of possible parameters in discrete steps, the resulting 1-dimensional χ^2 landscape should follow a parabolic shape. The result for the photon index is shown in Fig. 4.1, where such a parabolic shape is clearly visible with its minimum at the best-fit value. Another sign for the quality of the fits can be seen in the residuals. If the residuals show systematic deviations this is a bad sign for the modelling of the spectrum and indicate neglected model components. For the focal point of the data only statistical residuals can be seen. For the edges of the data range the quality of the model can not be evaluated, since the binning ranges span large energy ranges, due to low data counts. This leaves large uncertainties and could be either improved by specialized instruments which expand the effective area or longer observation times.

Due to the high overlap between the fitting parameters it is not possible to pick a likely scenario for the best inclination angle out of the X-ray analysis. Another attempt to gain insights into the physics of the blackhole was made by looking at the parameter space of the blackhole spin. This can be seen in Fig. 4.2 for the inclination angle of 47°. There it can be seen, that the χ^2 parameter space is far more complex, than the parameter space for the photonindex and that our global minimum lies beyond the boundary of the fitting interval. While a local minimum would be present it would lead to a false constraint of the spin parameter for wrong starting conditions. At the very least the χ^2

landscape indicates that a blackhole spin is most likely present, since there is no global minimum at 0.
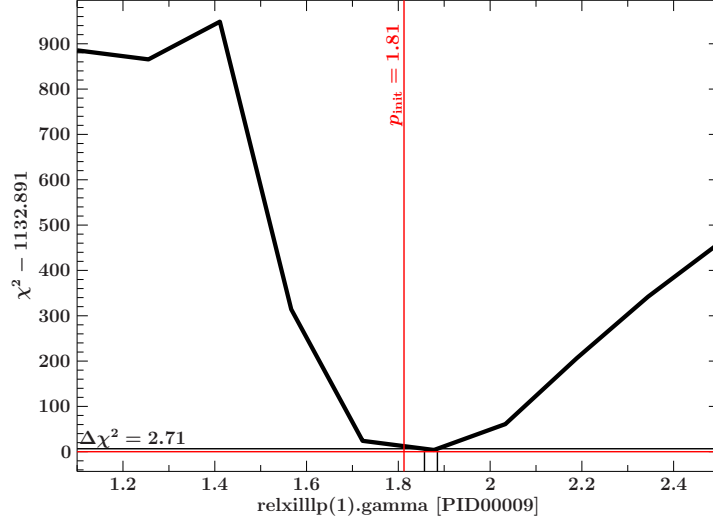
Figure 4.1.: Absolute χ^2 for the variation over the photonindex γ with 10 steps equidistant over the possible interval.

4.2. Kinematic Analysis

So far, three scenarios for the kinematic of the radio jet has been considered. The first presented in the analysis in Section 2.4, the one which tries to modify the association of components towards the model presented by Lister et al. (2018) and finally the model from Lister et al. (2018) itself. The X-ray models left no clear distinction which scenario is preferred, and from radio perspective only the second model could most propably neglected. While it is possible that components move towards the core, for example due to jet-bending, or show stationary behaviour, like shown by Jorstad et al. (2017) it is not very likely. The main issue lies in the linear fits as they show significant deviations, which can also be seen at the reducedχ^2. The scenario can not really convincingly be explained by linear moving components, which is why it is disregarded in the following. So, the only remaining valid scenarios are the one presented by Lister et al. (2018) and the first scenario presented in this analysis. Since multiple correct discrete Fourier-transformations of the visibilities can be found during the analysis of VLBI, both scenarios can be valid and more refined approaches are needed to find a distinction. An easy way to support a model is to include more data into the analysis. Hence, a new epoch observed during the work on this thesis in 2020, was included into the analysis. This epoch was imaged and model-fitted like the others and the consistency with the kinematic scenario one was tested. The imaging and modelfit-parameters can be found
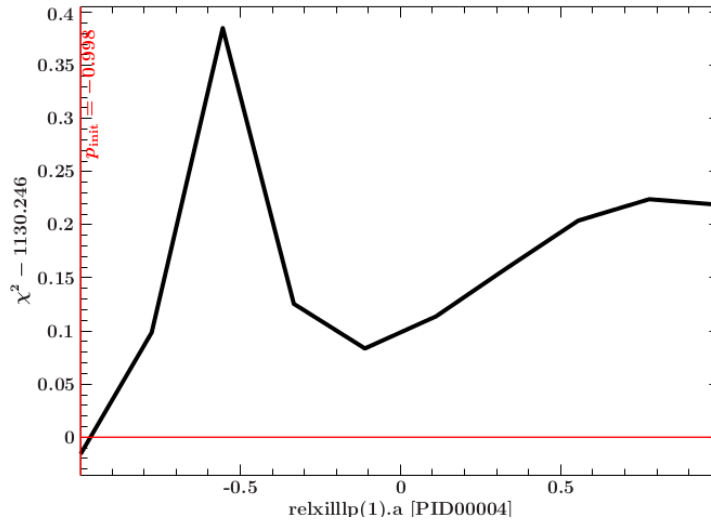
Figure 4.2.: Absolute χ^2 for the variation over the spinparameter a with 10 steps equidistant over the possible interval..

in Tab.A.1. The results of the imaging and modelfitting process are presented in Fig. 4.3. The implications on the distance to the core are shown in Fig.4.4, which shows a significant consistency to the scenario regarding the linear fits. A new discovery in this scenario would also be the newly ejected component, which is a valid possibility in steadily outwards moving jets. If this component proofs to be consistently detected in future observations this would make 2043+749 a perfect candidate to study the disk-jet coupling proposed by A. Marscher et al. (2002). The derived inclination angles of $\Phi = 47°$ for the first kinematic scenario presented in this thesis and the inclination angle derived out of the kinematic analysis of Lister et al. (2018) are consistent with the upper limit found by Pearson et al. (1992) for $\Phi < 49\,\text{deg}$.

The flux density of the source is continuous over the observed period with a slight increase to the later epochs. The flux density of the jet components is also pretty constant over all epochs. This also coincides with the observations in the X-ray regime shown by Lohfink et al. (2017), which compared X-ray flux densities measured by XMM-*Newton*, *Suzaku* and *NuSTAR* over the course of ten years for 2043+749 where almost no change in flux density was measured.

The brightness temperature of the core component is close to the inverse Compton limit of $T_{\text{b}} \sim 10^{12}\text{K}$. In 2018 the brightness temperature slightly exceeded, which could indicate stronger beaming effects and thus indicate towards a lower inclination angle, but this would have to proofed in future observations to get fully adopted. Since most minor axis of the core component diverged, the brightness temperature were only computed for three resolved core componens, which are too few data points to put a further constraint
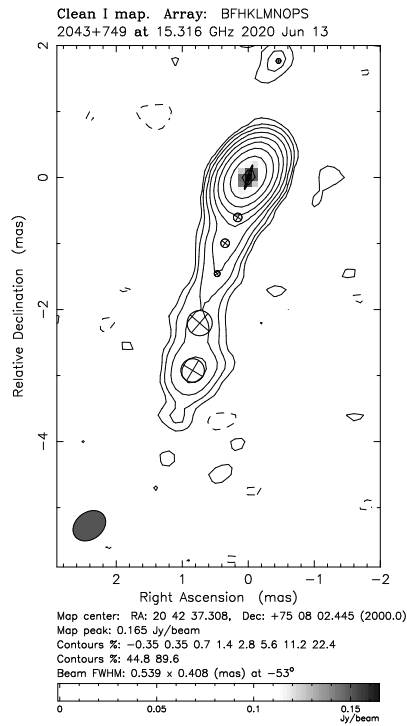
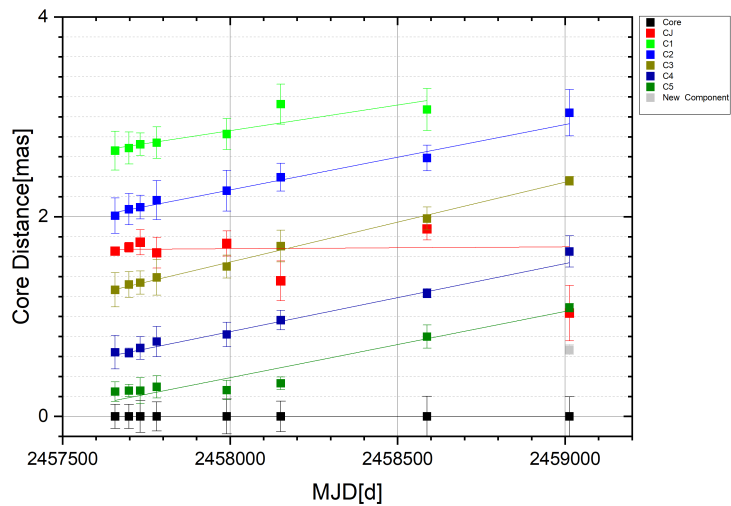**Figure 4.3.:** Radio image of 2043+749 in June 2020

Figure 4.4.: Distance to the core component with respect to the observation time with the new epoch observed on June 2020 with the VLBA.

on the inclination angle.

5. Summary and Outlook

In this thesis seven radio epochs of 2043+749 observed with the VLBA at 15 GHz were studied and put into perspective regarding the speed of the moving radio-jet components. According to three applied kinematic scenarios the highest components speed found in the jet where $\beta_1 = 1.89$, $\beta_2 = 0.76$, and $\beta_3 = 0.58$. The second model was proofed to be insufficient and thus only two models deemed to be valid candidates and thus resulting in an inclination angle of $\Phi_1 = 47°$ or $\Phi_2 = 18°$. Using a recent VLBA observation at 15 GHz and adding this epoch to the kinematic scenario presented in this thesis, a newly ejected component was found for the first scenario. All components showed an move outwards in the jet, with scenario one showing mildly superluminal features and scenario three, adapted from Lister et al. (2018), showed subluminal jet components. The flux density proofed to be very stable over the observed time frame.

An X-ray analysis was conducted on four *NuSTAR* observations analogue to Lohfink et al. (2017) and one *Swift*/XRT observation. The result yielded a slight difference in the goodness of fit with an original $\chi^2 = 1.0783$ in the fit by Lohfink et al. (2017) and $\chi^2 = 1.08917$ in the re-evaluation. The model in the X-ray analysis was then updated with the results of the radio inclination angles estimated from the VLBA data, but this showed very few effect on the model parameters derived from the new calculations. Therefore, it was not possible to further constrain the spin parameter of the blackhole with the newly acquired inclination angles.

The newly ejected component could proof a valuable asset in further studying the disk-jet interaction proposed by A. P. Marscher (2009), since this would make this a perfect candidate to further intensify X-ray observations of this source. This would be advantageous since radio observations of the VLBA are available due to the Mojave campaign. Also, the jet speed implies that further components will emerge at some given point, giving the opportunity to observe the predicted dips in the X-ray light curve.

Another observational aspect left for improvement is the uncertainty of the spectral index, since that has a considerable impact on the derived inclination angles. To improve this, the frequency bands used for observing has to be expanded by including more instruments in the monitoring. Moreover, with further observations it could be tested if the newly discovered component can be identified and tracked further observations, which would support one of the scenarios and also decrease the uncertainty of the component speeds.

Bibliography

Aleksic, Jelena, multi-wavelength partners multi-wavelength, and Joseph Moody (June 2011). "Fermi-LAT Observations of Markarian 421: the Missing Piece of its Spectral Energy Distribution". In.

Antonucci, Robert (Jan. 1993). "Unified models for active galactic nuclei and quasars." In: *araa* 31, pp. 473–521. DOI: 10.1146/annurev.aa.31.090193.002353.

Bach, Uwe (n.d.). *Pointing and Single Dish Amplitude Calibration Theory*.

Beckmann, Volker and Chris Shrader (2012). *Active Galactic Nuclei*. WYLEY-VCH. ISBN: 978-3-527-41091-0.

Bhatta, G. et al. (May 2018). "Signatures of the disk-jet coupling in the Broad-line Radio Quasar 4C+74.26". In.

Blandford, R. D. and A. Königl (Aug. 1979). "Relativistic jets as compact radio sources." In: *apj* 232, pp. 34–48. DOI: 10.1086/157262.

Blandford, R. D. and R. L. Znajek (July 1977). "Electromagnetic extraction of energy from Kerr black holes". In: *Monthly Notices of the Royal Astronomical Society* 179.3, pp. 433–456. ISSN: 0035-8711. DOI: 10.1093/mnras/179.3.433. eprint: https://academic.oup.com/mnras/article-pdf/179/3/433/9333653/mnras179-0433.pdf. URL: https://doi.org/10.1093/mnras/179.3.433.

Boettcher, Markus (June 2010). "Models for the Spectral Energy Distributions and Variability of Blazars". In: arXiv: 1006.5048 [astro-ph.HE].

Burke, Bernard F. and Francis Graham-Smith (2009). *An Introduction to Radio Astronomy*.

Cornwell Tim; Braun, Robert and Daniel S. Briggs (Jan. 1999). *Synthesis Imaging in Radio Astronomy II, Self-Calibration*. Vol. 180. Astronomical Society of the Pacific Conference Series.

Cornwell, Tim and Fomalont Ed B. (Jan. 1999). *Synthesis Imaging in Radio Astronomy II, Self-Calibration*. Vol. 180. Astronomical Society of the Pacific Conference Series.

Fanaroff, B. L. and J. M. Riley (May 1974). "The morphology of extragalactic radio sources of high and low luminosity". In: *mnras* 167, 31P–36P. DOI: 10.1093/mnras/167.1.31P.

Fomalont, Ed B. (Jan. 1999). *Synthesis Imaging in Radio Astronomy II, Self-Calibration*. Vol. 180. Astronomical Society of the Pacific Conference Series.

Garcia, J. et al. (Jan. 2014). "IMPROVED REFLECTION MODELS OF BLACK HOLE ACCRETION DISKS: TREATING THE ANGULAR DISTRIBUTION OF X-RAYS". In: *The Astrophysical Journal* 782.2, p. 76. ISSN: 1538-4357. DOI: 10.1088/0004-637x/782/2/76. URL: http://dx.doi.org/10.1088/0004-637X/782/2/76.

Gehrels, N. et al. (Aug. 2004). "The Swift Gamma-Ray Burst Mission". In: *apj* 611.2, pp. 1005–1020. DOI: 10.1086/422091. arXiv: astro-ph/0405233 [astro-ph].

Harrison, Fiona A. et al. (June 2013). "The Nuclear Spectroscopic Telescope Array (NuSTAR) High-energy X-Ray Mission". In: *apj* 770.2, 103, p. 103. DOI: 10.1088/0004-637X/770/2/103. arXiv: 1301.7307 [astro-ph.IM].

Hirsch, Maria (2019). *Roentgenbeobachtungen Schwarzer Loecher*.

Högbom, J. A. (June 1974). "Aperture Synthesis with a Non-Regular Distribution of Interferometer Baselines". In: *aaps* 15, p. 417.

Jorstad, Svetlana G. et al. (Sept. 2017). "Kinematics of Parsec-scale Jets of Gamma-Ray Blazars at 43 GHz within the VLBA-BU-BLAZAR Program". In: *The Astrophysical Journal* 846.2, p. 98. DOI: 10.3847/1538-4357/aa8407. URL: https://doi.org/10.3847/1538-4357/aa8407.

Kadler, Matthias (2015). *Extragalactic Jets*.

Kellermann, K. I. et al. (Oct. 1989). "VLA Observations of Objects in the Palomar Bright Quasar Survey". In: *aj* 98, p. 1195. DOI: 10.1086/115207.

Kembhavi, Ajit K. and Jayant V. Narlikar (1999). *Frontmatter*. Cambridge University Press, pp. i–iv.

King, Andrew (2008). "Disc accretion in active galactic nuclei". In: *New Astronomy Reviews* 52.6. Active Galactic Nuclei at the Highest Angular Resolution: Theory and Observations, pp. 253–256. ISSN: 1387-6473. DOI: https://doi.org/10.1016/j.newar.2008.06.006. URL: https://www.sciencedirect.com/science/article/pii/S1387647308001036.

Konigl, A. (Feb. 1981). "Relativistic jets as X-ray and gamma-ray sources." In: *apj* 243, pp. 700–709. DOI: 10.1086/158638.

Kovalev, Y. Y. et al. (Dec. 2005). "Sub-Milliarcsecond Imaging of Quasars and Active Galactic Nuclei. IV. Fine-Scale Structure". In: *aj* 130.6, pp. 2473–2505. DOI: 10.1086/497430. arXiv: astro-ph/0505536 [astro-ph].

Lesser, Michael (Nov. 2015). "A Summary of Charge-Coupled Devices for Astronomy". In: *Publications of the Astronomical Society of the Pacific* 127.957, pp. 1097–1104. DOI: 10.1086/684054. URL: https://doi.org/10.1086/684054.

Lister, M. L. et al. (Jan. 2018). "MOJAVE. XV. VLBA 15 GHz Total Intensity and Polarization Maps of 437 Parsec-scale AGN Jets from 1996 to 2017". In: *apjs* 234.1, 12, p. 12. DOI: 10.3847/1538-4365/aa9c44. arXiv: 1711.07802 [astro-ph.GA].

Lohfink, Anne M. et al. (May 2017). "The X-Ray Reflection Spectrum of the Radio-loud Quasar 4C 74.26". In: *The Astrophysical Journal* 841.2, p. 80. ISSN: 1538-4357. DOI: 10.3847/1538-4357/aa6d07. URL: http://dx.doi.org/10.3847/1538-4357/aa6d07.

Mannheim, K. (Mar. 1993). "The proton blazar." In: *aap* 269, pp. 67–76. arXiv: astro-ph/9302006 [astro-ph].

Marscher, A. P. (Sept. 2009). "Jets in Active Galactic Nuclei". In: *arXiv e-prints*, arXiv:0909.2576, arXiv:0909.2576. arXiv: 0909.2576 [astro-ph.HE].

Marscher, Alan et al. (July 2002). "Observational evidence for the accretion-disk origin for a radio jet in an active galaxy". In: *Nature* 417, pp. 625–7. DOI: 10.1038/nature00772.

Nandra, K. et al. (Nov. 2007). "An XMM-Newton survey of broad iron lines in Seyfert galaxies". In: *mnras* 382.1, pp. 194–228. DOI: 10.1111/j.1365-2966.2007.12331.x. arXiv: 0708.1305 [astro-ph].

Pearson, T. J. et al. (Nov. 1992). "A jet in the nucleus of the giant quasar 4C 74.26". In: *Monthly Notices of the Royal Astronomical Society* 259.1, 13P–16P. ISSN: 0035-8711. DOI: 10.1093/mnras/259.1.13P. eprint: https://academic.oup.com/mnras/article-pdf/259/1/13P/3514088/mnras259-013P.pdf. URL: https://doi.org/10.1093/mnras/259.1.13P.

Rybicki, George B. and Alan P. Lightmann (1985). *FUNDAMENTALS OF RADIATIVE TRANSFER*. John Wiley and Sons, Ltd. ISBN: 9783527618170. DOI: https://doi.org/10.1002/9783527618170.ch1. eprint: https://onlinelibrary.wiley.com/doi/pdf/10.1002/9783527618170.ch1. URL: https://onlinelibrary.wiley.com/doi/abs/10.1002/9783527618170.ch1.

Schwab, F. R. (Jan. 1980). "Processing of three-dimensional data". In: *1980 International Optical Computing Conference I*. Ed. by W. T. Rhodes. Vol. 231. Society of Photo-Optical Instrumentation Engineers (SPIE) Conference Series, p. 18. DOI: 10.1117/12.958828.

Seyfert, Carl K. (Jan. 1943). "Nuclear Emission in Spiral Nebulae." In: *apj* 97, p. 28. DOI: 10.1086/144488.

Shepherd, Martin (Mar. 2011). "Difmap: Synthesis Imaging of Visibility Data". In: *Astrophysics Source Code Library*, pp. 03001–.

Thompson Richard A.; Moran, James M. and George W. Swenson Jr. (2017). *Interferometry and Synthesis in Radio Astronomy*.

Turner, T. and L. Miller (2009). "X-ray absorption and reflection in active galactic nuclei". In: *The Astronomy and Astrophysics Review* 17, pp. 47–104.

Urry, C. Megan and Paolo Padovani (Sept. 1995). "Unified Schemes for Radio-Loud Active Galactic Nuclei". In: *pasp* 107, p. 803. DOI: 10.1086/133630. arXiv: astro-ph/9506063 [astro-ph].

Weedman, D W (July 1973). "Photometric study of Markarian galaxies". In: *Astrophys. J., v. 183, no. 1, pp. 29-39*. DOI: 10.1086/152205. URL: https://www.osti.gov/biblio/4304714.

Wehrle, AE et al. (Apr. 2001). "Kinematics of the Parsec-Scale Relativistic Jet in Quasar 3C 279: 1991-1997". In: *Astrophysical Journal Supplement Series - ASTROPHYS J SUPPL SER* 133, pp. 297–320. DOI: 10.1086/320353.

Wilms, J., A. Allen, and R. McCray (Oct. 2000). "On the Absorption of X-Rays in the Interstellar Medium". In: *apj* 542.2, pp. 914–924. DOI: 10.1086/317016. arXiv: astro-ph/0008425 [astro-ph].

Wolter, Hans (1952). "Spiegelsysteme streifenden Einfalls als abbildende Optiken fuer Rã¶ntgenstrahlen". In: *Annalen der Physik* 445.1â2, pp. 94–114. DOI: https://doi.

org/10.1002/andp.19524450108. eprint: https://onlinelibrary.wiley.com/doi/pdf/10.1002/andp.19524450108. URL: https://onlinelibrary.wiley.com/doi/abs/10.1002/andp.19524450108.

Zensus, A.J.; Diamond P.J. and P.J. Napier (Jan. 1995). *Very Long Baseline Interferometry and the VLBA*. Vol. 82. Astronomical Society of the Pacific Conference Series.

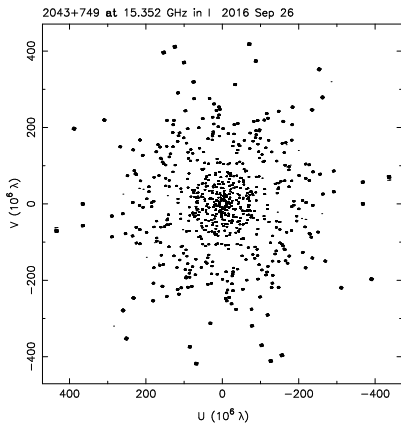# A. UV-coverage and Modelfitparameters

Table A.1.: Modelparameters for the radioobservations of 2043+749 with the VLBA

Date	S	Radius	Theta	amaj	P.A.	Tb
-	Jy	mas	deg	mas	deg	K
26-09-2016	0,161611	0,030939	-18,4681	0,243839	-23,7655	-
26-09-2016	0,0294907	0,274444	163,204	0,194333	56,31	163276525725,357
26-09-2016	0,00868234	2,02962	162,855	0,352844	62,1027	48618843192,11
26-09-2016	0,00915119	1,26739	162,207	0,342683	60,9454	51566533104,0002
26-09-2016	0,00679544	0,655501	164,856	0,333735	45	54253714512,6747
26-09-2016	0,00929001	2,68675	163,144	0,387917	36,8699	40246636082,9907
26-09-2016	0,00138074	1,64653	-16,6241	0,0709836	-18,4349	1193423953644,11
06-11-2016	0,172291	0,0323397	-23,9397	0,242256	-21,6541	-
06-11-2016	0,0307643	0,274272	159,658	0,125479	56,31	392068964912,407
06-11-2016	0,00923531	2,05626	162,723	0,312794	62,1027	61896920853,2068
06-11-2016	0,00948559	1,28527	161,921	0,256343	60,9454	92180821798,9723
06-11-2016	0,0085414	0,674381	164,564	0,0913445	45	725354441807,346
06-11-2016	0,00934072	2,68548	163,257	0,319627	36,8699	59284351846,6822
06-11-2016	0,00155389	1,67619	-14,0202	0,0956016	-18,4349	658034244638,499
10-12-2016	0,16343	0,026942	-19,2527	0,322176	-20,263	-
10-12-2016	0,0220906	0,255491	161,312	0,256347	56,31	93221428640,7923
10-12-2016	0,00873215	2,12146	162,629	0,239174	62,1027	105818500305,172
10-12-2016	0,00897586	1,36592	162,784	0,230315	60,9454	114140612062,569
10-12-2016	0,00701234	0,709288	163,392	0,228618	45	115637033010,985
10-12-2016	0,00725748	2,75027	163,358	0,225819	36,8699	118547564821,764
10-12-2016	0,0010072	1,7185	-16,3262	0,251173	-18,4349	95283587844,44
28-01-2017	0,16406	0,029476	-24,3626	0,292557	-21,7951	965712072548,123
28-01-2017	0,0265719	0,275777	160,452	0,222354	56,31	124396222839,905
28-01-2017	0,0094032	2,15375	162,419	0,391372	62,1027	39543204580,477
28-01-2017	0,00945369	1,36612	161,631	0,358475	60,9454	47136063662,7597
28-01-2017	0,00870648	0,724882	162,132	0,303972	45	65510717346,4736
28-01-2017	0,00718622	2,74921	163,116	0,31366	36,8699	61442300845,3337
28-01-2017	0,00131444	1,63814	-9,21255	0,308947	-18,4349	62996551834,4118
28-01-2017	0,00528932	5,93852	166,496	7,83297	-15,0407	-
25-08-2017	0,209257	0,0303158	-23,9484	0,349555	-20,2124	-
25-08-2017	0,0274551	0,296097	158,279	0,193493	56,31	164401474258,04
25-08-2017	0,0110626	2,2406	163,048	0,407862	62,1027	36464617317,827
25-08-2017	0,00857174	1,47025	162,004	0,228932	60,9454	115481899656,654

25-08-2017	0,00930992	0,802462	163,154	0,245505	45	100483393972,245
25-08-2017	0,00449589	8,0049	164,176	7,64381	-20,5897	-
25-08-2017	0,00799468	2,83312	164,111	0,310275	36,8699	62835929046,1031
25-08-2017	0,00100293	1,75778	-10,7313	0,252415	-18,4349	94347850430,609
02-02-2018	0,225912	0,0325424	-21,1952	0,303757	-20,2322	1698813699597,84
02-02-2018	0,0311424	0,338492	160,657	0,126709	56,31	384622174294,779
02-02-2018	0,0109432	2,33548	163,06	0,280433	62,1027	77124685640,2521
02-02-2018	0,00894458	1,63583	161,495	0,319318	60,9454	59378009871,2023
02-02-2018	0,00163285	0,789076	-9,84859	0,00350149	70,3462	490573463971317
02-02-2018	0,00755161	3,04904	163,961	-	59,37	-
02-02-2018	0,00927199	0,887307	163,48	-	45	-
02-02-2018	0,00456856	9,2628	160,054	10,5397	-26,9468	-
02-02-2018	0,0018595	1,6451	-17,8196	0,397455	57,5288	38082278368,0519
02-02-2018	0,0011605	2,6751	-14,0024	0,347815	70,821	49696709997,2697
15-04-2019	0,237051	0,00169916	-31,2841	0,401261	-21,1481	517087152728,692
15-04-2019	0,00996898	2,58507	162,941	0,256187	73,3007	92333185941,2546
15-04-2019	0,00460046	1,97347	160,558	0,230373	74,7449	113634655168,059
15-04-2019	0,00849896	3,06102	164,181	0,420111	45	34290230718,8087
15-04-2019	0,00164343	1,86611	-15,328	0,222953	160346	121000551096,178
15-04-2019	0,0069486	1,2479	162,314	0,0928781	75,9637	700593688795,763
15-04-2019	0,00857556	0,835376	162,327	0,230647	63,435	113771319481,994
13-06-2020	0,212767	0,00211369	-33,819	0,394207	-18,0789	710491749345,946
13-06-2020	0,00420974	1,08511	160769	0,0860557	51,3402	814069679124,267
13-06-2020	0,00422018	1,64917	163420	0,313858	30,9638	61201004157,2648
13-06-2020	0,00846446	3,03895	163320	0,463399	59,0362	28182197922,1381
13-06-2020	0,00741853	1,03516	-16,4195	0,554799	32,6192	19642881366,3488
13-06-2020	0,00274077	0,666245	161328	0,103725	148610	559600277821,782
13-06-2020	0,00208953	2,35823	161938	0,088276	49,3987	772153935181,618

(a) 26-09-2016
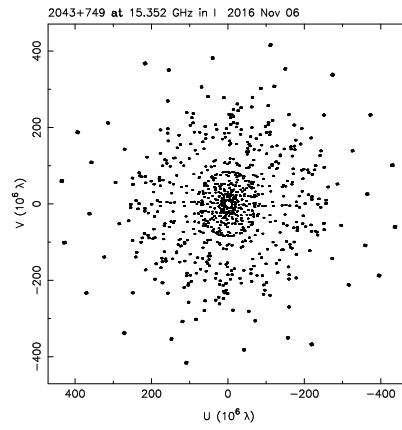
(b) 06-11-2016
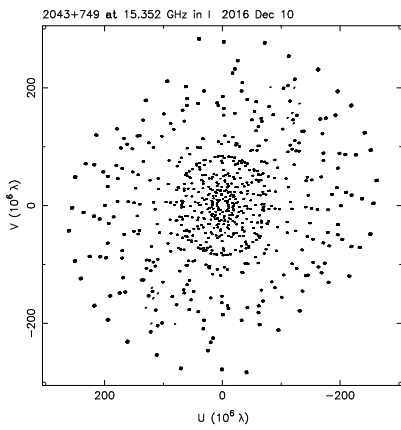
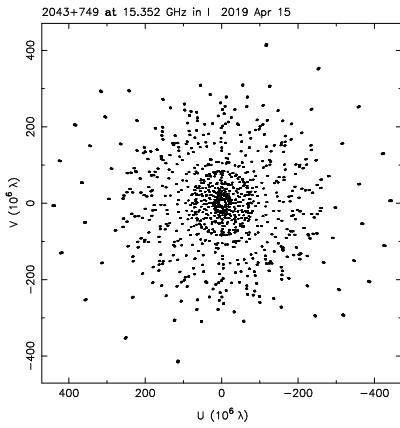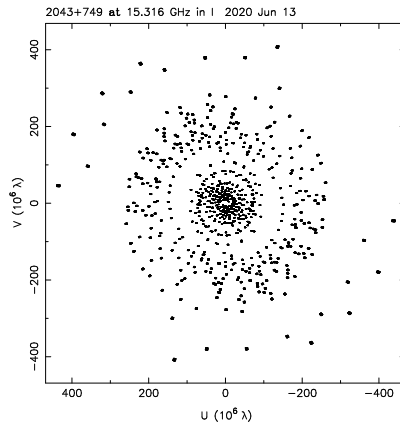**(c)** 10-12-2016
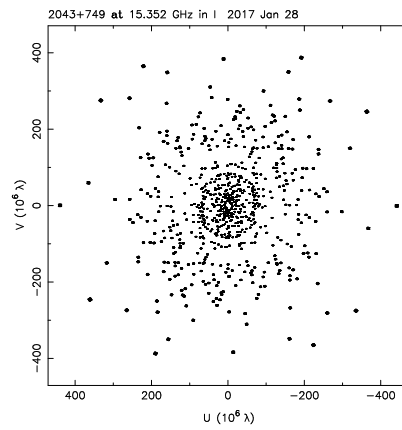
(d) 28-01-2017
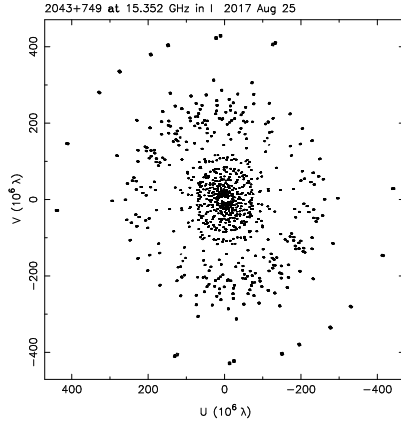
(e) 25-08-2017
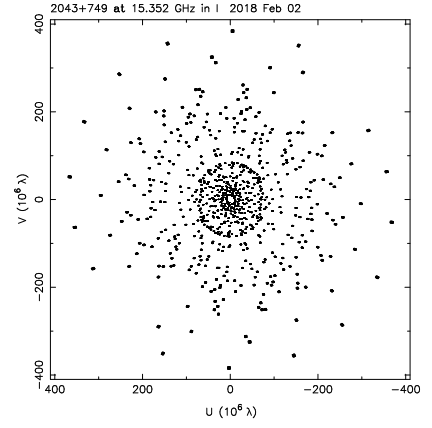
(f) 02-02-2018

(g) 15-04-2019

(h) 03-06-2020

Figure A.1.: (u,v)- coverage of all eight epochs observed with the VLBA at 43 GHz

Danksagung/Acknowledgement

Zum Abschluss moechte ich mich bei allen bedanken, die mich unermuedlich auf dem Weg zu dieser Arbeit begleitet haben.

Dies ist zuerst Prof. Dr. Matthias Kadler, der den Anstoss dieses spannenden Projektes gegeben hat und mich mit den vielen aufkommenden Problemen immer durch hilfreiche Ratschlaege oder spannende Diskussionen weitergebracht hat. Er hat mit den Einfuehrungsvorlesungen mein Interesse in die Astrophysik geweckt und mich ueber weite Teile des Studiums begleitet.

Desweiteren moechte ich mich Andrea Gokus bedanken, die mit vielen Hinweisen und Diskussionen, insbesondere zum Roentgenteil, ebenfalls viel zu dieser Arbeit beigetragen hat.

Ich moechte mich bei Florian Roesch bedanken, der ebenfalls mit vielen hilfreichen Ratschlaegen, mich durch diese Arbeit begleitet hat. Er hat mich ebenfalls durch weite Teile des Studiums begleitet und hatte als Buerokollege Anteil an vielen spannenden Diskussionen.

Ich moechte mich bei Prof. Dr. Karl Mannheim bedanken, dem Inhaber des Lehrstuhls und Ko-Betreuer, der mit fuer dieses grossartige Umfeld in der Astronomie verantwortlich ist.

Ich moechte mich bei allen Mitgliedern der AG Kadler bedanken, die mit ihrer offenen Art, auch in den derzeit bedingten Online-Groupmeetings, viele hilfreiche Fragen und Diskussionen angestossen haben. Fuer diese tolle Arbeitsatmosphaere bin ich dankbar.

Ich will mich bei allen Coffee-Breaklern bedanken, die auch in turbulenten Zeiten etwas Normalitaet zulassen und viele coole Gespraeche ermoeglichen.

Zuallerletzt moechte ich mich bei meiner Familie bedanken, meinen Eltern und der Familie meines Bruders, die mich durch mein gesamtes Studium und darueber hinaus immer unterstuetzt haben. Vielen Dank an alle!